8-2014

Study of ferroelectric oxides and field effect in complex oxides heterostructures

Lu Jiang
University of Tennessee - Knoxville, ljiang3@vols.utk.edu

To the Graduate Council:

I am submitting herewith a dissertation written by Lu Jiang entitled "Study of ferroelectric oxides and field effect in complex oxides heterostructures." I have examined the final electronic copy of this dissertation for form and content and recommend that it be accepted in partial fulfillment of the requirements for the degree of Doctor of Philosophy, with a major in Physics.

Takeshi Egami, Major Professor

We have read this dissertation and recommend its acceptance:

Hanno Weitering, Elbio Dagotto, David Mandrus, Honyung Lee

Accepted for the Council:

Carolyn R. Hodges

Vice Provost and Dean of the Graduate School

(Original signatures are on file with official student records.)

Study of ferroelectric oxides and field effect in complex oxides heterostructures

A Dissertation Presented for the
Doctor of Philosophy
Degree
The University of Tennessee, Knoxville

Lu Jiang
August 2014

ACKNOWLEDGEMENT

This dissertation is accomplished under the advisory of my supervisor Dr. Takeshi Egami and co-advisor Ho Nyung Lee. I wish to show my most gratitude to them. Their wisdom and their creative thinking has been my source of inspiration throughout this work. Beyond technical guidance, their professional attitudes benefit me so much during my entire Ph. D. years. I truly appreciate it for all their patience and their time for mentoring me from the very beginning of my graduate years, both academically and mentally. I want to thank them for all their supports to my Ph. D. career.

I would also like to express my sincere gratitude to my committee member Dr. Elbio Dagotto. His classes and his seminars give me very profound understanding on material science and good training as a researcher. Also, I want to thank his cooperation on my work in the theoretical part. I want to thank my committee member Dr. David Mandrus and Dr. Hanno Weitering for accepting my invitation to be my Ph. D. committee members and thank for all their suggestions and comments on the comprehensive meeting. I enjoy our discussions and feel glad to be able learn from them.

I would like to thank Oak Ridge National Lab for providing me with advanced experimental instruments and inspiring academic atmosphere, which is quite helpful for my research. I also want to thank all the kind and passionate colleagues in the thin film group. They help me with details of my experiments, discussions and manuscript writing, and without their help, this work is impossible to be finished successfully. In addition, I want to thank all the friends and classmates in University of Tennessee for their supports and sharing joy with me. I really have a wonderful graduate student life with them.

Finally, I would like to thank my parents for giving me the opportunity of growing up with love and happiness. I want to show my gratitude for their cares and encouragements on me. Although I have to stand on myself in a foreign country, the greetings and supports from the other side of the earth can still warm me. Moreover, I want to thank my husband, for his sharing his life with me. His supports and encouragements is also important for me and brighten my everyday life.

ABSTRACT

With the rapid development of technology, the need for novel materials and state-of-the-art devices is growing fast. Complex oxides which have strongly correlated electrons are favorable candidates for materials industry, due to their rich phase diagrams and multiple functions. Especially, ferroelectric oxides is very promising materials in the industry for storage, due to their bistable polarization states triggered by external electrical field. This thesis is centered on ferroelectric oxides, analyzing their lattice structures and investigating the interface of ferroelectrics and other complex oxides to examine the potential of the heteostructures in the application in electronic devices.

The most notable feature of ferroelectric oxides is their reversible spontaneous polarization, which is strongly related to the lattice distortion in the crystal. In chapter 2, we report a neutron diffraction study of $NaNbO_3$ [sodium niobate], to comprehensively understand the origin of ferroelectricity. We find that the structure evolves six phases from 930K to 15K in long-range, while only three real ground states are detected at short-range.

We then study the ferroelectric/manganites heterostructures and explore its potential in the application in field effect transistors and ferroelectric memories. In chapter 3, we first describe the insulator-to-metal phase transition is realized in $La_{0.8}Sr_{0.2}MnO_3$ [strontium doped lanthanum titanate oxides] under the field-effect of the ferroelectric $Pb(Zr_{0.2}Ti_{0.8})O_3$ [lead titanate oxides] layer. Moreover, we find that the interfacial transition plays a very crucial role in the tunneling electroresistance effect (TER) of the heterostructures.

In chapter 4, we test the similar function at the interface of ferroelectrics and cuprates. We describe that the epitaxial strain and oxygen stoichiometry both lead to substantial changes in superconducting properties and these two factors are strongly coupled. And we demonstrate that the interface superconductivity is achieved in overdoped cuprates $La_{1.6}Sr_{0.4}CuO_4$ [strontium doped lanthanum cuprate oxides] under field effect, with high Meissner volume and T_c [superconducting transition temperature] around 15K. Therefore, our results provide deep understanding on ferroelectric materials and open more opportunities for their application.

TABLE OF CONTENTS

LISTS OF FIGURES

CHAPTER 1

INTRODUCTION

Growing interests have been attracted to complex oxides due to their coupling of electronic, magnetic, thermal, mechanical, and optical properties, which promises their broad applications in various technologies and devices in industry. Moreover, novel phenomena and multifunctionality can appear at the interfaces of oxides thin film, especially the interface of ferroelectrics and complex oxides, in which the field effect manipulates various novel electronic and magnetic properties. So this work mainly focuses on the structure and physical properties of ferroelectric oxides and its application in field effect based electronic devices.

Materials

Background of complex oxides

Complex transition metal oxides span a wide range of crystalline structures which makes it an intriguing topic in the world of physics. Most transition metal oxides belong to strongly correlated electron oxides ascribed to the incompletely filled d- and f-electron shells with narrow bands. In this class of materials, the interplay of charge, spin, orbital and lattice degrees of freedom generates rich spectra of phases and novel physical functionalities, including ferroelectricity, ferromagnetism, insulator-to-metal transitions, high-temperature superconductors and so on. This motivated our extensive investigation with the aim of understanding of existing materials and exploration of advanced materials for future. In this thesis, we mainly focus on ferroelectrics, manganites oxides and cuprate superconductors.

Cuprate superconductors

The first high temperature superconductors (HTSC) were discovered in copper oxides in 1986 by IBM researchers Georg Bednorz and K. Alex Muller.[1] After this major breakthrough in the field of superconductivity (SC), a number of perovskite cuprates superconductors, especially $YBa_2Cu_3O_6$ (YBCO)[2] and $Bi_{2-x}Sr_xCa_2CuO_2$ (BSCCO)[3], were discovered. These compounds have critical temperatures above the boiling point of liquid nitrogen, forming the basis of a current large technological interest. The goal of realizing room temperature superconductors has attracted extensive attempts; but up till now, the highest superconducting transition temperature is reported to be 133 K for the compound $HgBa_2Ca_2Cu_3O_{8+x}$,[4] and whether room temperature SC is possible or not is still an open question.

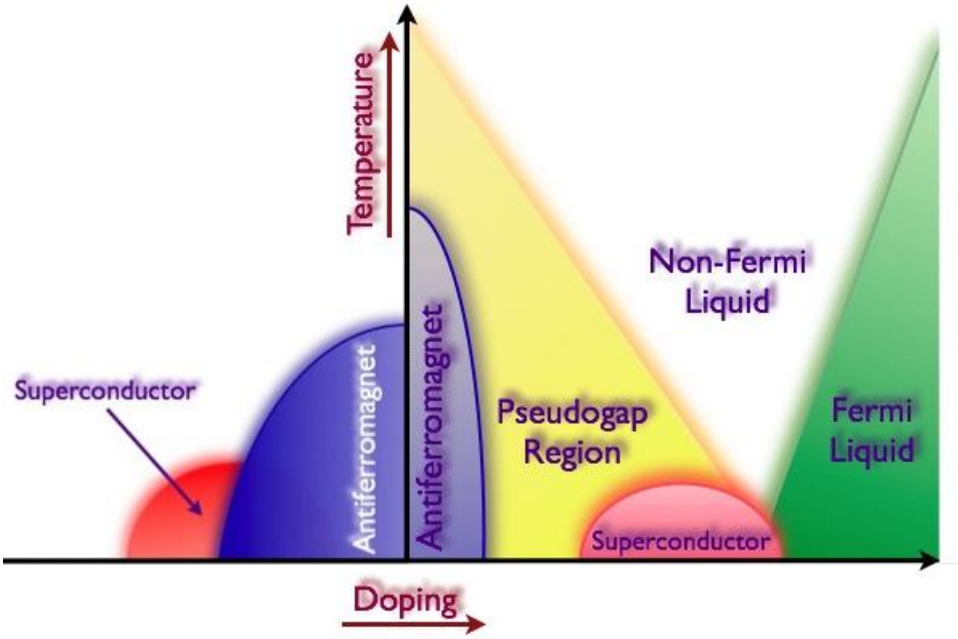

Figure 1. Phase diagram of doped cuprate oxides.

The left part is for hole doping and the right part is for electron doping.

The high temperature superconductors found in copper oxides compounds usually evolves from the “Mott” insulators, when carriers are doped into the crystals, as shown in figure 1. The key element for all these structures is the CuO_2 plane, whose occupancy of carriers determines the ground state. In a Mott insulator, the virtual charge fluctuations generate super-exchange interaction, which favors antiparallel alignment of neighboring spins. As carriers are inserted into CuO_2 plane, the strong correlation between electrons coupled them into “Coulomb pairs” and results in superconductivity. Although the electron-electron interaction has been generally confirmed as the origin for high-temperature superconductivity, the underlying mechanism has been a controversial topic for more than two decades.

The simplest high-temperature cuprates are the single-layer compounds derived from the parent material La_2CuO_4 (LCO)[5]. LCO is an antiferromagnetic insulator, but the HTSC can be obtained by both electron and hole doping. The Sr substituted compound (LSCO), in which the electrons removed from a filled band to make hole carriers, is one of the most often studied HTSCs. The spin configuration plays an important role in $La_{2-x}Sr_xCuO_4$ (LSCO) structure. Above x=0.02, the long-range magnetic order is destroyed, but two-dimensional short range spin correlations appear, which results in spin glass states. The system behaves like a 2D disordered metal with a gradual change from a metal at high temperatures to an insulator at low temperatures. Superconductivity appears at x=0.05, and the Tc can reach its highest point, 40K, at x=0.15.

For this compound, multiple properties and physical origins have been studied through various methods. For instance, the superconductivity of LSCO can be enhanced, even created by epitaxial strain[6,7] or excessive oxygen[8,9], in which abnormally high Tc (Tc=50K) can be achieved. Spin and charge inhomogeneities, which refers to the "stripe" in cuprates have been detected by local structure from neutron scattering and nuclear magnetic resonance[10]; Fermi surface and band structure have been studied by angular resolved photoemission spectroscopy[11]; phase stiffness and pesudogap have been shown in some theoretical calculations[12,13], and so on. In this thesis, we mainly focus on the creation of superconductivity by the field effect. To fully realize and understand the coupling in ferroelectrics and cuprates, we start from the well-known strain induced superconductivity and interface influence on SC.

Manganite oxides

Manganite oxides have the general formula $Re_{1-x}A_xMnO_3$, in which Re is a trivalent rare earth element (Re=La, Pr, Nd, Sm, Eu, etc) and A is a divalent alkaline earth element (A=Ba, Sr, Ca, etc). These compounds are in perovskite structures (ABO_3) as shown in figure 2a, with mixture of Re and A in A sites and Mn in B sites. The Mn atom has an electronic configuration $1s^2 2s^2 2p^6 3s^2 3p^6 3d^5 4s^2$, with unfilled *d* orbital shell. When Re is substituted by A, a part of Mn^{3+} will convert into Mn^{4+} valence state to maintain the charge neutrality of the system. In $Re_{1-x}A_xMnO_3$ crystal lattice, the 5-fold orbital degeneracy of the 3*d* levels of Mn is split into the lower-lying triply degenerate t_{2g} states and the higher-lying doubly degenerate e_g states, as shown in figure 2b. So a Mn^{3+} ion has an electronic configuration $3d^4$ with 3 electrons at the t_{2g} orbitals and 1 electron at the e_g orbitals, in which S=2. And a Mn^{4+} is in $3d^3$ electron configuration, with three t_{2g} electrons and no e_g electrons, in which S=3/2.

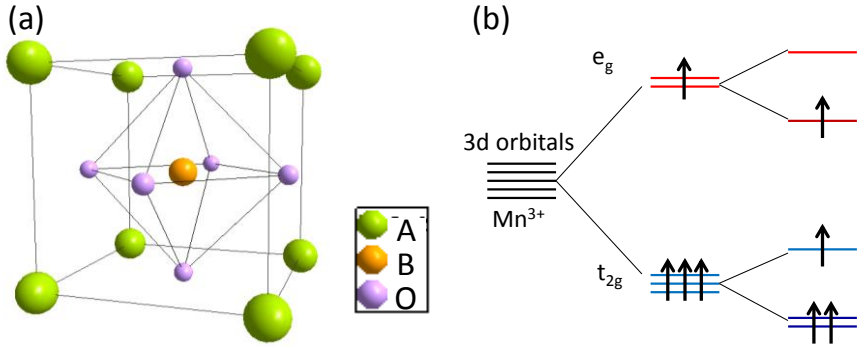

Figure 2. Structure of perovskites and spin configuration for manganites
(a) ABO_3 cubic perovskite unit cell (b) Splitting of e_g and t_{2g} orbitals of Mn^{3+} due to Jahn-Teller distortion.

In the $Re_{1-x}A_xMnO_3$ lattice, when the symmetry of the MnO_6 octahedron is lowered, the Jahn-Teller distortion can further split the t_{2g} and e_g levels. Since Mn^{4+} ion does not have e_g electrons, the energy remains unchanged, whereas the energy of e_g occupied

state of Mn^{3+} is changed due to the Jahn-Teller distortion. So in manganites which have high concentration of Mn^{3+} ions, Jahn-Teller distortion has a strong tendency to take place, leading to lowering of the lattice symmetry.

The magnetic properties of the manganites are dominated by the exchange interactions between the magnetic moments of Mn ions. In doped manganites, two Mn states coexist: Mn^{3+} with one e_g electron and Mn^{4+} with no electron at e_g level. The double exchange interaction between ions in different valence states, in which an e_g electron localized at a Mn^{3+} ion can hop onto the vacant place of a neighboring Mn^{4+} ion, results in metallic conductivity and ferromagnetism. However, the superexchange interactions between two similar Mn ions, in which virtual electron hopping happens at the next-to-nearest neighbors, promises the manganites become insulator and antiferromagnet. These two exchange mechanisms coexist and govern the electronic and spin states in the manganites.

One of the most studied doped manganites is $La_{1-x}Sr_xMnO_3$, which has a rich and complex phase diagram, as shown in figure 3. It evolves from a spin-canted insulator to a ferromagnetic insulator and then a ferromagnetic metal and finally into an antiferromagnetic insulator. So, different ground states compete with increasing x. Theoretical calculations have revealed that phase separation into ferromagnetic and antiferromagnetic regions spreads through the whole structure in manganites. Since the phase separation and the competition of various electronic and magnetic ground states are rather sensitive to external stimulus, we carried out the field effect study on manganites and explored the application of manganites heterostructures in transistors and memories in this thesis.

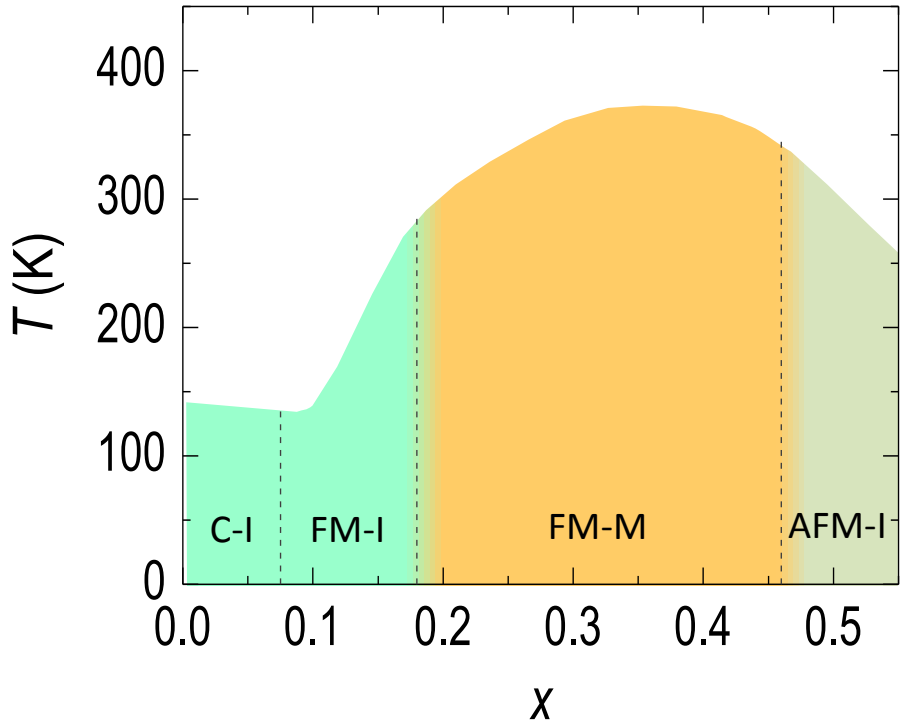

Figure 3. Phase diagram of $La_{1-x}Sr_xMnO_3$.
CI, FM, AFM, I and M correspond to spin-canted, ferromagnetic, antiferromagnetic, insulator and metal, respectively.

Ferroelectrics

The first discovery of ferroelectricity is traced back to the observation of the nonlinear electrical properties in potassium sodium tartrate tetrahydrate ($KNaC_4H_4O_6$)[14], which is already well known as a piezoelectric compound several decades ago. However, it has not attracted sufficient attention at that time due to the suppression of this phenomenon by a very small deviation from the chemical stoichiometry. When a new type of ferroelectric oxides, barium titanate $BaTiO_3$, was discovered[15], intensive interests have been born on this kind of materials. It was a very important achievement because $BaTiO_3$ was the first ferroelectric structure without hydrogen bonds and had more than one ferroelectric phase. After this discovery, a number of perovskite ferroelectric oxides began to be found rapidly. Then, a Bi-based layered structure oxides joined the family of ferroelectrics with high dielectric permittivity and good retention[16]. In nowadays, more than one thousands ferroelectric materials are known. They are widely used in the application for capacitors, transistors, sensors and so on.

Ferroelectricity is intimately connected with interesting and important electronic phenomena, including piezoelectricity (the coupling of electrical and elastic properties)

and pyroelectricity (the coupling of electrical behaviors with temperature). But the most prominent feature of ferroelectrics is the reversibility of its permanent polarization, which results in a hysteresis loop in the dependence of polarization *P* on electric field *E.* So the magic of ferroelectric materials is operating it at the scale of a unit cell, in which a spontaneous electric polarization can be switched by an external electric field, resulting in bistable states. Moreover, ferroelectric crystals have a Curie temperature, below which the structure is able to become polar and the electric dipole can form.

Due to strong polarization, good response and multiple phases, perovskite oxides become the most popular member in the ferroelectric family. The perovskite structure has the chemical composition ABO_3, with a corner positioned atom (0, 0, 0) (B-site) and a body centered atom (1/2, 1/2, 1/2) (A-site). In ferroelectric perovsite oxides, the atom's off-centered displacement and order-disorder transition will result in a spontaneous polarization. Most ferroelectric crystals consist of domains and the boundaries between two neighboring domains are called domain walls. In absence of an external electric field, the domains are randomly arranged. When the electric field is applied, the domains will be oriented along the field direction. Therefore, the domain dynamics and the domain-wall motion are the essential factors to determine dielectric, piezoelectric, pyroelectric, and ferroelectric properties and hence are a subject of extensive scientific research.

In order to detect the origin of ferroelectricity, the lattice distortion and domain structure are the key parameters. Structural determination is usually carried out by X-ray or electron diffraction. The Bragg peaks obtained from diffraction patterns can accurately determine the lattice symmetry and lattice constant when the crystal structure is perfect. But the ferroelectric phase is usually accompanied by local distortion, and the local bond length varies from the prediction from the average structure.[17] Therefore, we introduce local structure investigations on ferroelectric materials to have a deeper understanding on the origin of the spontaneous polarization in this thesis.

Applications

Ferroelectric field effect transistor

A ferroelectric transistor is evolved from a field-effect transistor (FET), which is a transistor that uses an electric field to control the conductivity of a channel of one type of charge carrier in a semiconductor material. In a ferroelectric field effect transistor, the metal gate has been replaced by a ferroelectric layer; and this produces a device with nondestructive readout in which the polarization of the gate could be sensed simply by monitoring the magnitude of the source-drain current. In order to improve the performance of a ferroelectric FET, stronger polarization, better retention of ferroelectric materials, and advanced design of the transistors have been developed all these years.

While besides ferroelectric materials, modulating the semiconductor channel materials is also a functional method to improve the FET performance. Especially, when the traditional silicon channel is replaced by complex oxides, the polarization in ferroelectric gate can introduce drastic carrier population change which results in huge difference in drain currents. For complex oxides, as we mentioned above, the strong electron correlations lead to various novel phases. Under the field effect from ferroelectrics, the carrier densities of these correlated electron oxides can be drastically tuned, and possibly results in metal-to-insulator, antiferromagnet-to-ferromagnet, and insulator-to-superconductor transitions, as shown in figure 4.[18] In this thesis, we realized the phase transition of insulator-to-metal and antiferromagnet-to-ferromagnet in the ferroelectric/manganite oxides heterostructures; and also discovered the Fermi liquid to superconductor transitions in the ferroelectric/cuprate oxides heterostructures.

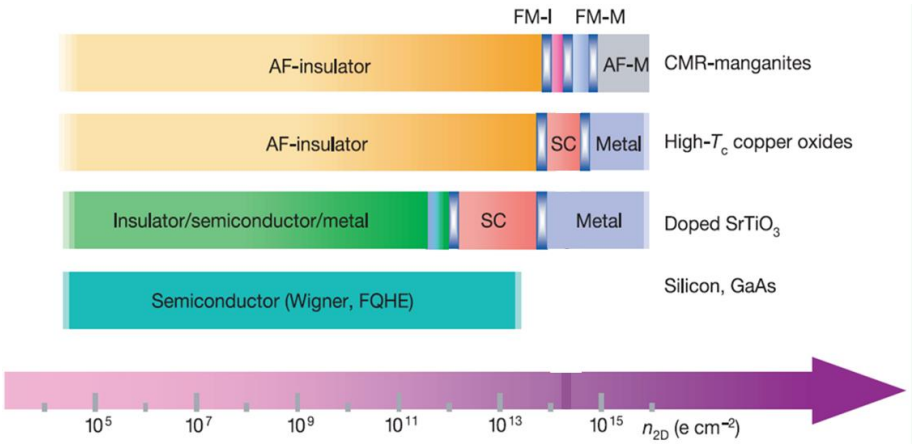

Figure 4. Phase diagrams of complex oxides.

Ferroelectric memories

Ferroelectric memories originate from the idea that the electronic information can be stored in the electrical polarization in ferroelectrics. When a ferroelectric layer is sandwiched by electrodes, the tunneling electroresistance depending on the two orientations of ferroelectric polarization can determine the states in the memories.[19-21] The barrier to develop the ferroelectric memories is the technique to fabricate ultrathin ferroelectric layer which can still maintain the strong polarization and fast response. With the development of ferroelectric materials and thin film synthesis technologies, nowadays the difficulty of thickness limit has been overcome by advanced ferroelectric materials, such as lead zirconate titanate (PZT) which can sustain its polarization even in a few unit cells.[22]

After a group of experimental and theoretical attempts on ferroelectric tunnel junction to understand the electroresistance effect, several factors have been considered to contribute to the resistance switching by polarization orientation: the different

incomplete carriers screening at the boundaries of ferroelectrics and the electrodes; the atoms' displacement and reconstruction at the interface which results in different transmission possibility; the strain from the piezoelectricity applied to the ferroelectric barrier which tunes the transport characteristics of the barrier, as shown in figure 5.[23] In this thesis, we explore more mechanisms of electroresistance effect and introduce more parameters to the ferroelectric memories as a result.

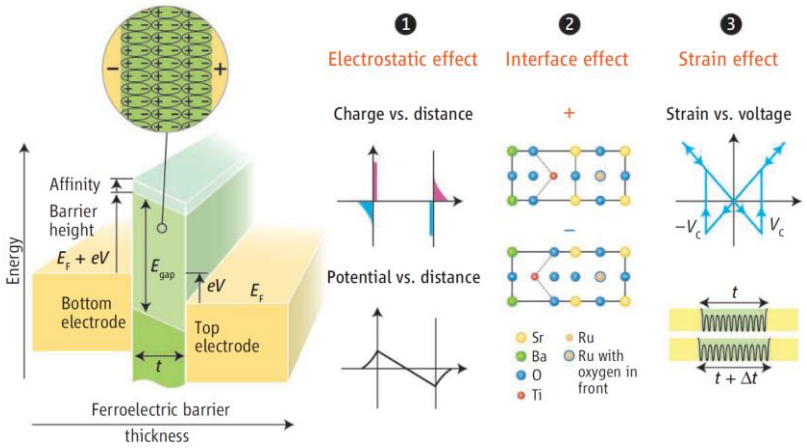

Figure 5. Structure and mechanism of ferroelectric tunnel junction

Schematic viewgraph of a ferroelectric tunnel junction which consists of two electrodes separated by a few nm-thick ferroelectric barrier layer.

CHAPTER II

LOCAL STRUCTURE OF FERROELECTRIC OXIDES

In order to achive comprehensive understanding of the physical properties and develop practical application of ferroelectrics, a deep knowledge of the lattice structure and the origin and formation of the spontaneous polarization of ferroelectrics is needed. So we first focus on the refined structural analysis of ferroelectric oxides in this chapter.

Introduction

Ferroelectric materials are widely used in many electromechanical components and electronic devices, such as actuators, sensors, field-effect transistors, and ultrasonic transducers. Due to strong piezoelectric response, $Pb(Zr,Ti)O_3$ (PZT) is the most widely employed ferroelectric material at present, even though lead has recently been banned from many commercial applications and materials, for example, from solder, glass, and pottery glaze, due to concerns regarding its toxicity. Therefore a concerted effort was mounted to develop lead-free piezoelectric ceramics. A large number of studies have been focused on the discovery of better ferroelectrics near the morphotropic phase boundaries (MPB) in alkaline niobate based perovskite solid solutions.[24–26] In particular Saito, et al.[4] have designed a new lead-free ferroelectric based on the MPB in the

data to probe the local structure of each phase and details of each phase of $NaNbO_3$. perovskite-rich region of $(K,Na)NbO_3$, which shows excellent piezoelectric performance comparable to those of PZT. Interestingly, their mother compound, sodium niobate, $NaNbO_3$, is known for its complex phase behavior, and there are a number of conflicting reports on its structure.[28–43] Thus there is a strong need for understanding the structure and phase transformation of sodium niobate.

At high temperatures, $NaNbO_3$ takes the structure of simple perovskite. But as the temperature is lowered,[28–30] pressure is applied[31] or the sample size is reduced,[32] $NaNbO_3$ undergoes a surprisingly complex sequence of structural phase transitions. Its rich phase diagram is generally described by Glazer and Megaw,[33] which contains at least six phases, varying from cubic at high temperature, through tetragonal, orthorhombic, and, finally, to rhombohedral structure below room temperature. This complexity invited many scientists to study the temperature-induced phase changes in $NaNbO_3$ and its soft mode mechanism for structural change.[28,31,34–38] However, the results are seriously contradictory to each other, particularly at low temperatures. Above 913 K, it has a paraelectric cubic phase *Pm3m*, and when cooling down, it evolves through a series of antiferrodistortive phases, tetragonal (T_2) *P4/mbm*, orthorhombic (T_1) *Cmcm*, orthorhombic (*S*) *Pbnm*, orthorhombic (*R*) *Pbnm*, orthorhombic (*P*) *Pbcm*

phases, and forms a rhombohedral *R3c* phase at low temperatures. Mishra et al. replace the space group *Pnmm* of *S* and *R* phases with the *Pbnm* group according to a high-resolution powder neutron diffraction study.[39] They also point out that the antiferroelectric phase *Pbcm* and the ferroelectric phase *R3c* coexist and have competing interaction at room temperature and below.[40] Further in the transition mechanism, the high and room-temperature phase transitions are considered to be due to the NbO_6 octahedral tilting, while the low-temperature transitions are related to the off-centered displacements of niobium atoms and octahedral distortions of NbO_6.[41–43] In spite of extensive use of experimental techniques and theoretical studies, surprisingly large amounts of controversies are still present on the details of the structure and process of phase transitions of $NaNbO_3$. In this part, we use the Rietveld and pair distribution function (PDF) analyses of high-resolution neutron scattering.

Results and Discussions

Rietveld analysis of powder neutron diffraction data

Powder sample of $NaNbO_3$ (99.997% purity) was purchased from Alpha Aesar Co., and the pulsed neutron diffraction measurements were performed with the NPDF spectrometer of the Lujan Center of Los Alamos National Laboratory at various temperatures. The results were first analyzed using the Rietveld refinement (EXRGUI, revision 1225). The neutron diffraction pattern at 930K shown in Figure 6 was analyzed on the basis of an ideal cubic structure with the space group *Pm3m*. The cubic phase is well fitted with the structural parameters of the ideal perovskite, with Na at (0,0,0), Nb at (0.5,0.5,0.5), O at (0.5,0.5,0) and $a = b = c = 3.9507$ Å. All the Bragg reflections present could be indexed as main cubic perovskite reflections. When temperature is lowered to 880 K, the appearance of the superlattice peaks shown in Figure 6 indicates the phase transition to the tetragonal *P4/mbm* space group, which is induced by *M* and *R* zone boundary condensation involving the rotation of NbO_6 octahedral. Between 820 and 770K, $NaNbO_3$ has an orthorhombic *Cmcm* space group phase. The appearance of additional superlattice peaks (see Figure 6) is the sign for phase transition and multiplicity of the unit cell. When the temperature further goes down, numerous controversies are drawn on the space groups and phase transitions. As the temperature falls in the range of 700–600 K, Ahtee et al.[29] find that it belongs to the *Pnmm* space group symmetry with the cell dimensions 2 × 2 × 2 with respect to the elementary perovskite cell by X-ray diffraction measurements. However, Mishra et al. argue that it undergoes a phase transition to the *Pbnm* space group with the $\sqrt{2} \times \sqrt{2} \times 12$ cell dimensions at 700 K and $\sqrt{2} \times \sqrt{2} \times 6$ cell dimensions at 600 K through neutron diffraction measurements. Our neutron diffraction patterns can be fitted well by the *Pbnm* space group parameters with $\sqrt{2} \times \sqrt{2} \times 6$ cell dimensions, partly supporting Mishra et al., but not much difference is seen between the patterns for 700 and 600 K. Note that our model includes a small portion (4.5%) of a phase with *Cmcm* space group at 700 K.

Between room temperature and 490 K, the orthorhombic *Pbcm* space group seems to achieve the best fit in the Rietveld refinement. Below room temperature, as detected by Mishra et al., the orthorhombic *Pbcm* group and rhombohedra *R3c* group coexists within the entire temperature range, including the lowest temperature. When we compare every peak at low and room temperatures, it seems that most of the supperlattice peaks at low temperatures can find their original formation at room temperature, in spite of some shifts in the Q value and changes in intensity, still, some peaks are an exclusive result of the *R3c* space group symmetry, as shown in Figure 7. The evolution of phase transitions in our Rietveld refinement is shown in Table I and the lattice parameters, parameters of every atom position, thermal factor, phase fraction, and the agreement factors are shown in Table II. The definition of parameters in the table can be found in Ref. 44.

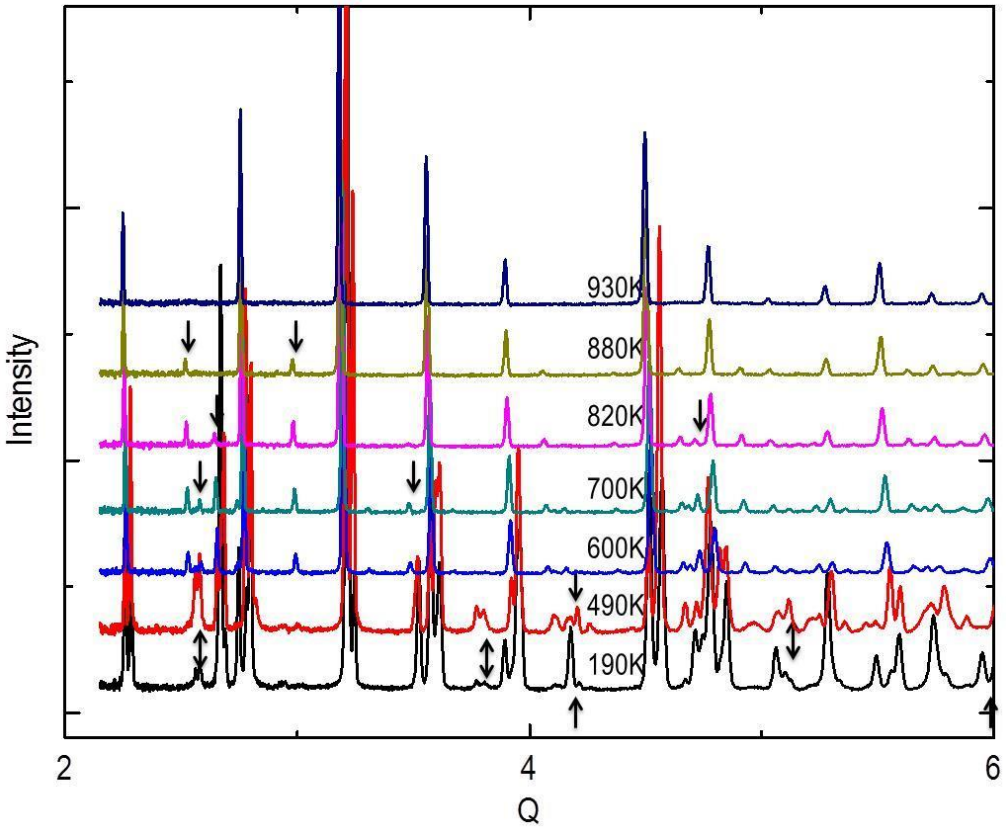

Figure 6. Diffraction patterns of $NaNbO_3$

Evolution of the neutron diffraction patterns for $NaNbO_3$ as temperature is varied from 930 to 15K. Each pattern is representative for one phase of $NaNbO_3$. Superlattice peaks are marked with arrows.

Pair distribution function analysis above room temperature

In the antiferroelectric and ferroelectric phases, $NaNbO_3$ undergoes lattice distortion, with tilting and atomic off-center displacements in the short range. However, the diffraction patterns are not sensitive to detailed local displacements during the phase transition. In order to determine differences between the local and average structures, the PDF method was employed to probe the evolution of the local structure, especially for those at temperatures below 490 K. The PDF, denoted $g(r)$ in the following formula, describes all the interatomic distances present in the structure, and is obtained from the total structure function $S(Q)$ through the Fourier transformation[45]

$$g(r)-1=\frac{1}{2\pi^2 r\rho_0}\int_0^{+\infty} Q[S(Q)-1]\sin(Qr)dQ$$

Because *S(Q)* includes both the Bragg and diffuse scattering intensities the PDF can describe aperiodic as well as periodic structure. From 900K to 600K, the PDF calculated (PDFGUI 1.0b) with the fitting parameters same as those in the Rietveld analysis shows good agreement with the experimental PDF, indicating that the crystallographic structure provides also a good description of the local atom arrangement above 600K. Figure 8 is an example of the experimental PDF agreeing with the calculated PDF using the Rietveld model at 820K. In Figure 8, within the basic cubic perovskite cell (around 4 Å), the two primary peaks correspond to Nb-O and Na-O are at r = 1.9 Å and r = 2.8 Å, which indicates that Nb is at the center of an NbO_6 octahedron and there is no obvious distortion in the unit cell.

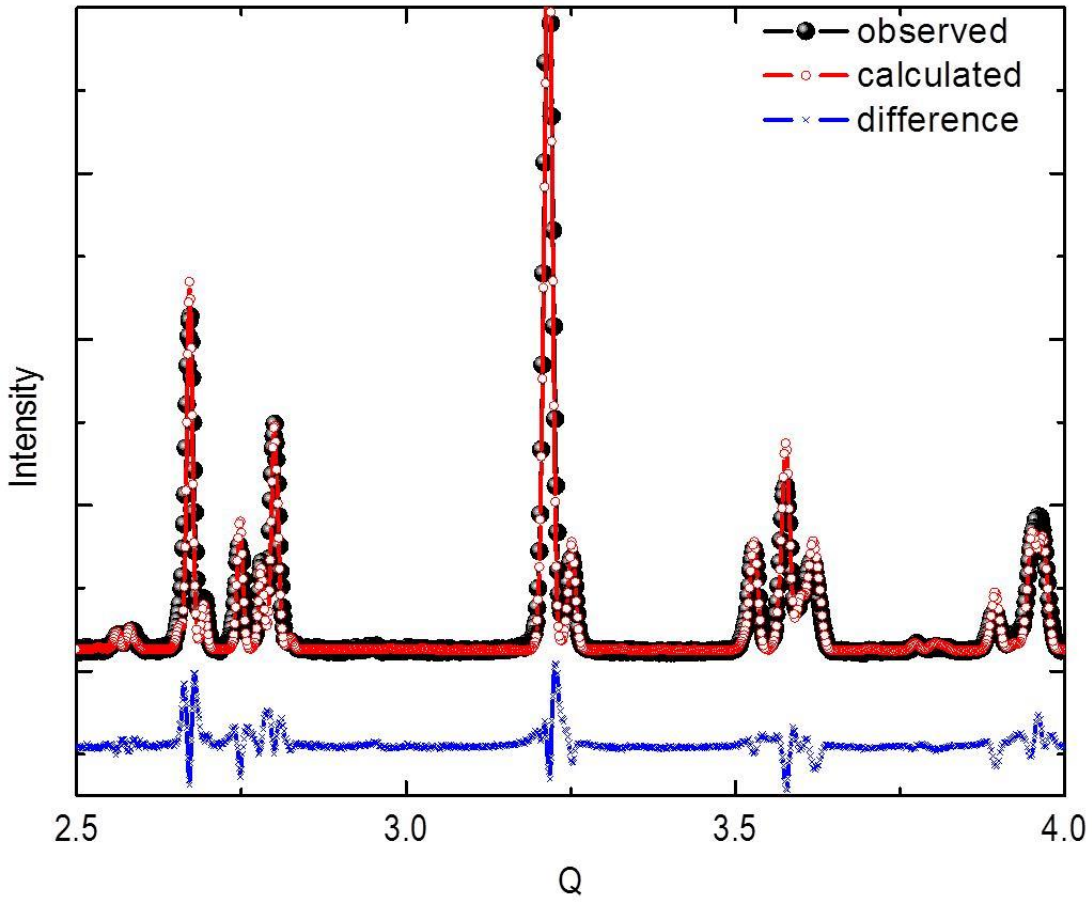

Figure 7. Diffraction fitting of $NaNbO_3$
Observed (solid spheres), calculated (open circles), and difference (crosses) profiles obtained after the Rietveld refinement of $NaNbO_3$ using the mixture of phaseswith rhombohedra *R3c* group (70%) and orthorhombic *Pbcm* group (30%) at 15 K. Peaks marked with arrows are the ones belong only to the *R3c* group according to the analysis of GASA software.

TABLE I. Phase evolution of NaNbO3 at various temperatures

Temperature	Space group	Symmetry
930K	Pm3m	Cubic
880K	P4/mbm	Tetragonal
820-770K	Cmcm	Orthorhombic
700K	Cmcm+Pbnm	Orthorhombic
600K	Pbnm	Orthorhombic
490-300K	Pbcm	Orthorhombic (AFE)
190-15K	Pbcm+R3c	Rhombohedra (FE)

When temperature is lowered to 490K, through the PDF analysis we find that the structure model obtained by the Rietveld refinement actually shows very poor agreement at small *r*, as shown in Figure 9, which suggests that for $r < 5.2$ Å the structure is actually not in the *Pbcm* space group. The PDF provides the data for true atomic distances which cannot easily be determined from the average structure analysis by the Rietveld analysis. If we use the parameters for the low temperature phase *R3c* group to refine all the atom positions and thermal factors, we can get excellent fit to the PDF below 5.2 Å as shown in Figure 10. The same conclusion is obtained through the PDF fitting from 490K to 300K. Therefore, in this range of temperature, the *Pbcm* space group describes only the long-range symmetries and atomic positions. On the other hand within the short range up to 5.2 Å, the correct local structure is surprisingly the *R3c* space group. This size of the domain is slightly smaller than the rhombohedral *R3c* unit cell, in which it keeps the character and symmetry of the *R3c* group, though distorted. These small *R3c* domains gradually stack into the *Pbcm* space group through the entire structure. Depending on the models resulted from the Rietveld refinement, the *a* and *b* axis of the *Pbcm* unit cell rotate by 45° from those of the *R3c* unit cell; so it is most likely that the atoms form twin structures (as the Na and O atoms shown in figure 11) in *R3c* domains and along its diagonal direction, the whole structure can result in *Pbcm* symmetry. Moreover, the *R3c* space group is a ferroelectric phase while the *Pbcm* space group is antiferroelectric, which means that the local domains in the *R3c* group has a spontaneous polarization and they align in antiparallel arrangements to revolve into the *Pbcm* group. Along the *c* axis, the length of the *Pbcm* unit cell ($c = 15.48$ Å) is about twice as the *R3c* unit cell ($c = 7.82$ Å) and about four times as the elementary cubic cell (3.95 Å), so every basic polarized cell also form similar twin structures to make the polarizations stack antiparallel through the whole structure as shown in Figure 11.

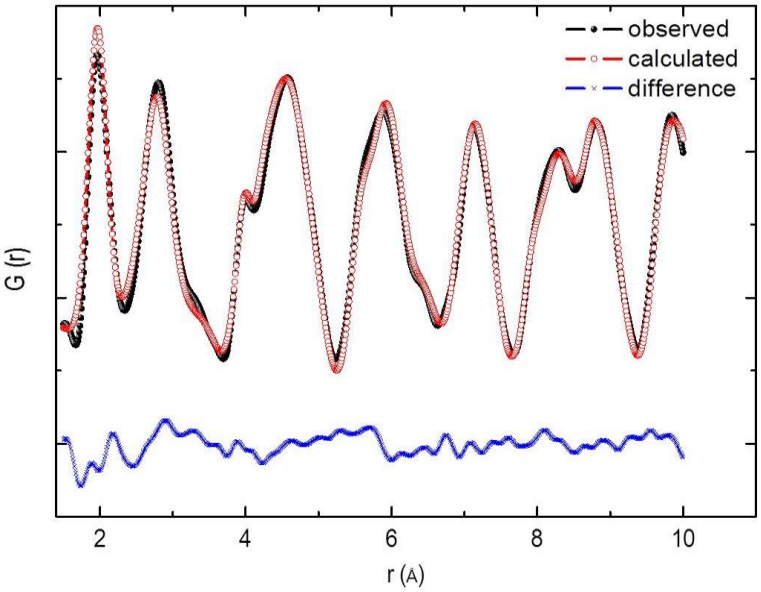

Figure 8. Local structure fitting of $NaNbO_3$ at 820K

Neutron pair distribution function *G*(*r*) analysis of $NaNbO_3$ at 820 K with the *Cmcm* parameters from the Rietveld analysis. This phase is well described by the *Cmcm* structure. Models obtained by the Rietveld analysis can fit the PDF from 930 to 600 K quite well. This is an example that shows the accuracy of the Rietveld model at high temperatures.

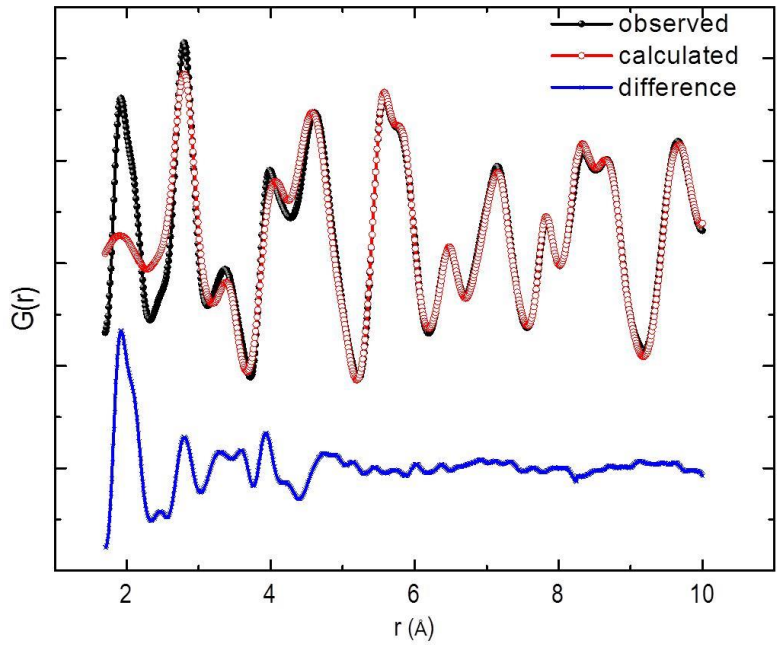

Figure 9. Local structure fitting of $NaNbO_3$ at 490K

Neutron pair distribution function *G*(*r*) analysis of $NaNbO_3$ at 490 K with the *Pbcm* group. Note that this structure model can describe the PDF only above 5.2 Å.

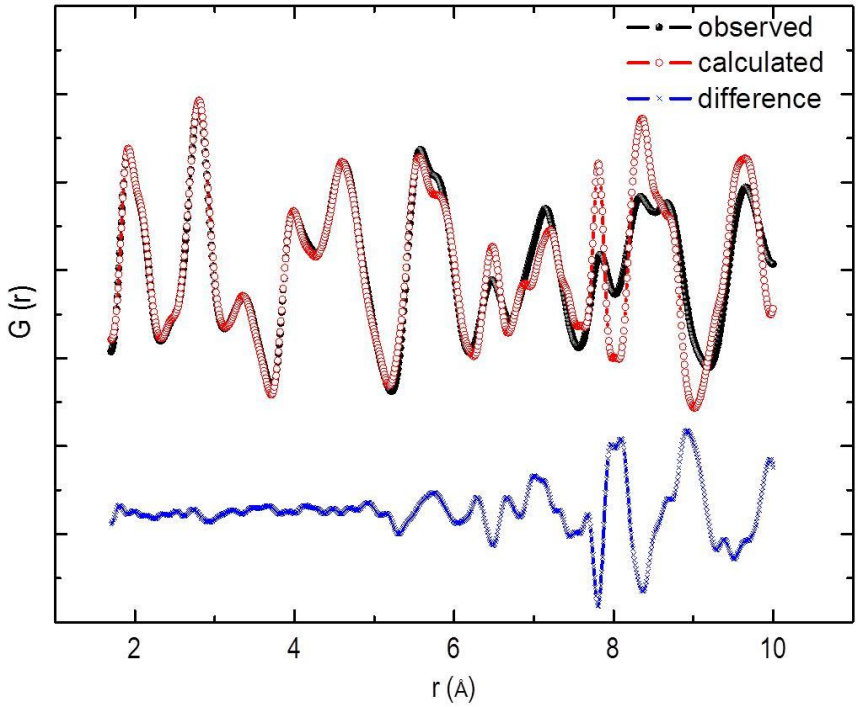

Figure 10. Local structure fitting of $NaNbO_3$ at 490K
Neutron pair distribution function $G(r)$ analysis of $NaNbO_3$ at 490 K with the *R3c* group. Note that this phase can describe the structure profile only below 5.2 Å.

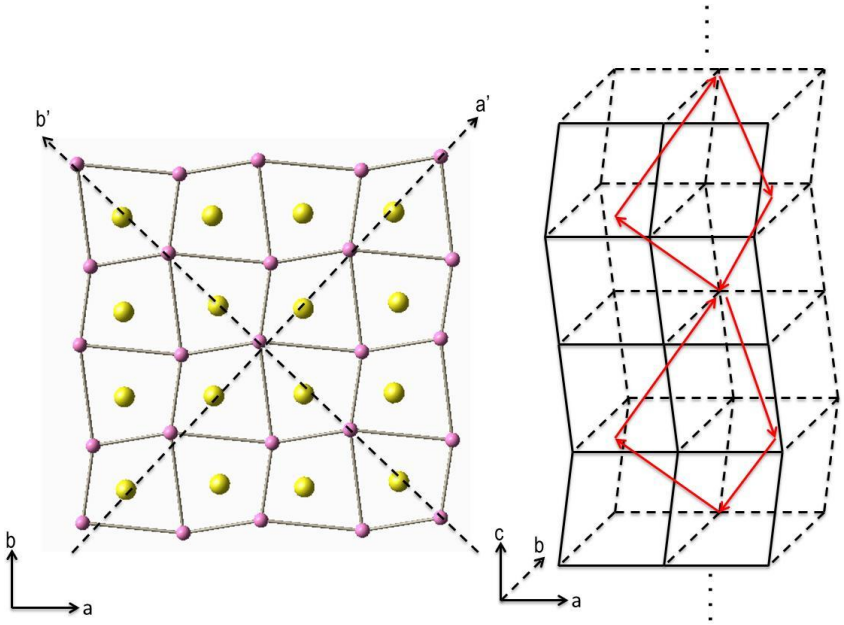

Figure 11. Structure of $NaNbO_3$ at 490K in short range
(a) Atomic arrangement of NaNbO3 at 490 K. Yellow balls are Na, green balls are niobium, and purple balls are oxygen. ***a'*** and *b'* are *R3c* axes and *a* and *b* are *Pbcm* axes. (b) Construction of the basic cells (~4 Å) and local polarizations. Every arrow corresponds to a spontaneous polarization in an elementary perovskite cell.

It is traditionally considered that the spontaneous polarization in ferroelectric and antiferroelectric phases of $NaNbO_3$ originates from the distortion of the lattice and off-centered displacement of Nb atoms. Figure 12 shows the PDF of $NaNbO_3$ at a very short range, which is within the range of an elemental perovskite unit cell from 930 to 15K. We can see that the first peak, which corresponds to the Nb-O bond, is broad and asymmetric but without a split down to 600K (six green curves shown in Figure 12). As temperature falling down to 300K (four blue curves shown in Figure 12), the peak due to Nb-O bond is separated into two subpeaks, one around r = 1.9 Å and the other around r = 2.1 Å , and a Na-O bond peak appears at r = 2.4 Å as well. When the temperature is above 600 K, where the structure is paraelectric, the Nb-O bond length is 1.95 Å and the Na-O bond length is 2.8 Å. Therefore, in the antiferroelectric phases, the Nb atom in the octahedral NbO_6 is off-centered by 0.15 Å or 7.7%, while the Na atom in NaO_8 is off-centered by 0.4 Å or by 14%. This means Na has even a larger off-centered displacement than Nb, as shown in Figure 13, and both displacements contribute to the formation of local dielectric polarization.

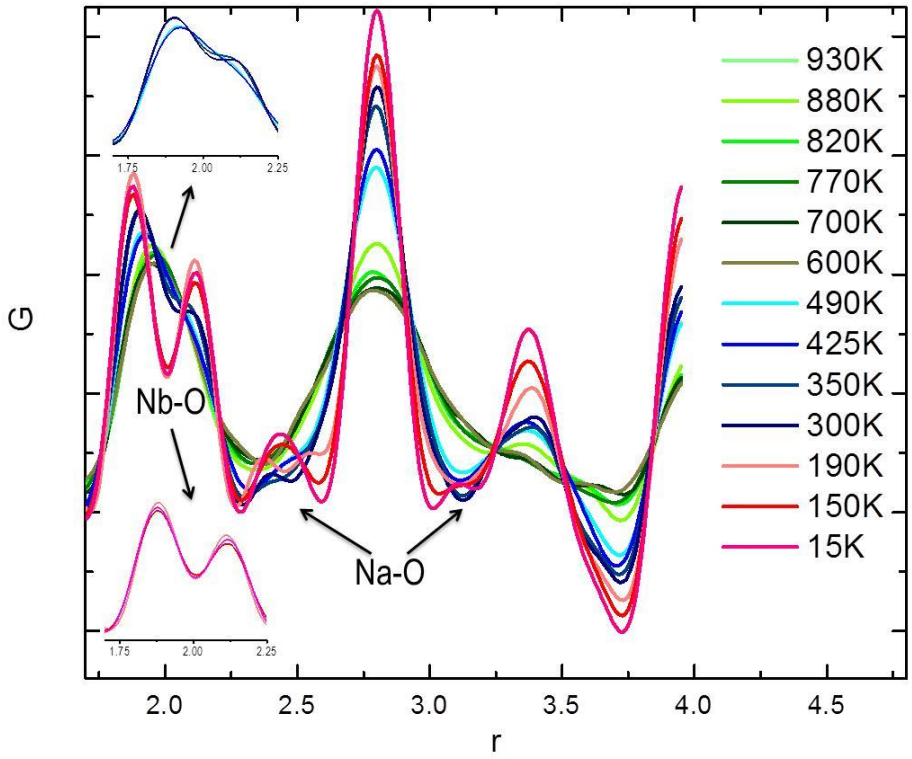

Figure 12. Pair distribution function of $NaNbO_3$

Neutron pair distribution function *G*(*r*) analysis of $NaNbO_3$ from 930 to 15 K up to 4 Å. Note that the result can be divided into three groups with the evolution of temperature: 900–600K (green lines), 490–300K (blue lines), and 190–15K (red lines). This indicates that only two basic structural changes happen at a short range. Peaks resulted from Na-O and Nb-O bonds are marked with arrows and obvious Nb-O bond lengths changes at very short distance from 490 to 15K are also emphasized in the inset.

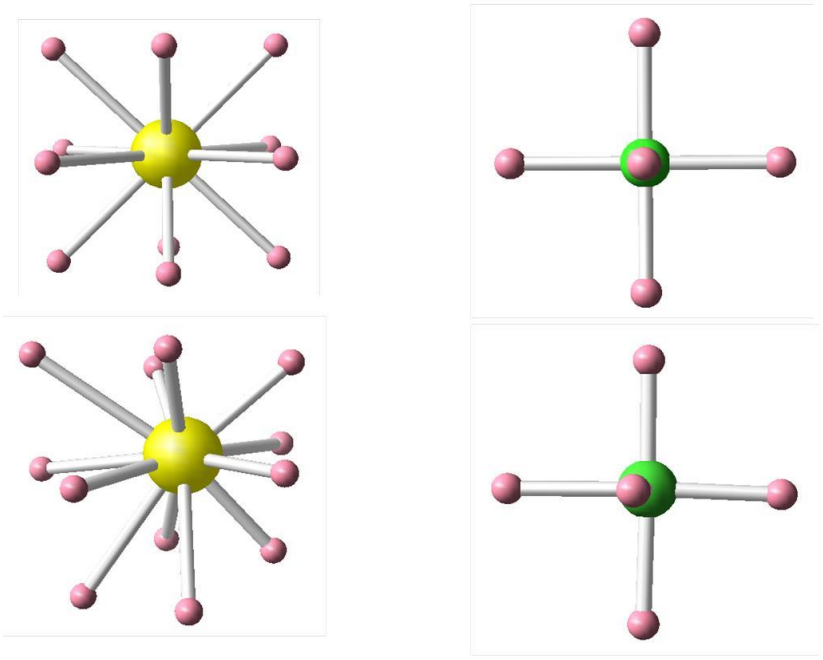

Figure 13. Atom arrangements of NaO_{12} and NbO_6
Depictions of NaO_{12} at 930K (left top) and at 15K (left bottom), and NbO_6 at 930K (right top) and at 15K (right bottom) according to the PDF analysis. Na and Nb displacements are exaggerated for clarity.

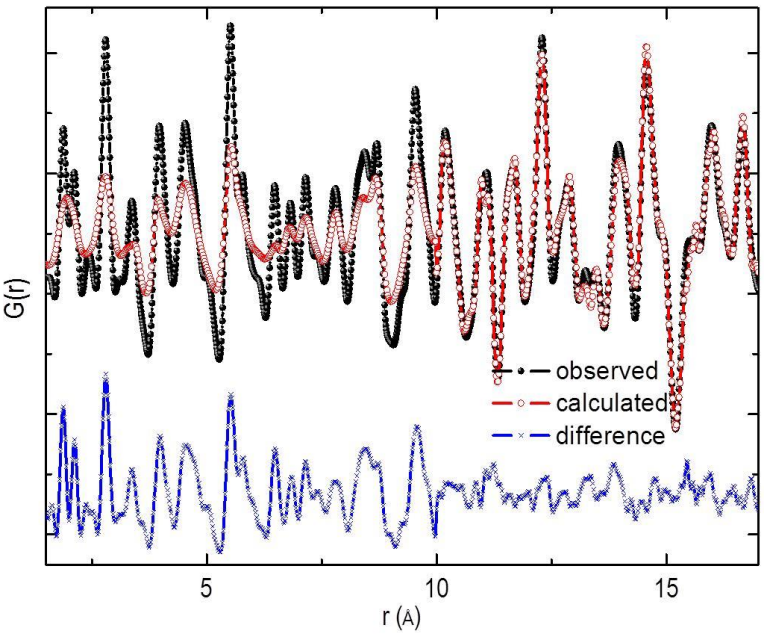

Figure 14. Local structure fitting of $NaNbO_3$ at 15K
Neutron PDF analysis of $NaNbO_3$ at 15K with *R3c* and *Pbcm* group coexistence model from the Rietveld analysis. Note that the differences gradually vanish above 10 Å.

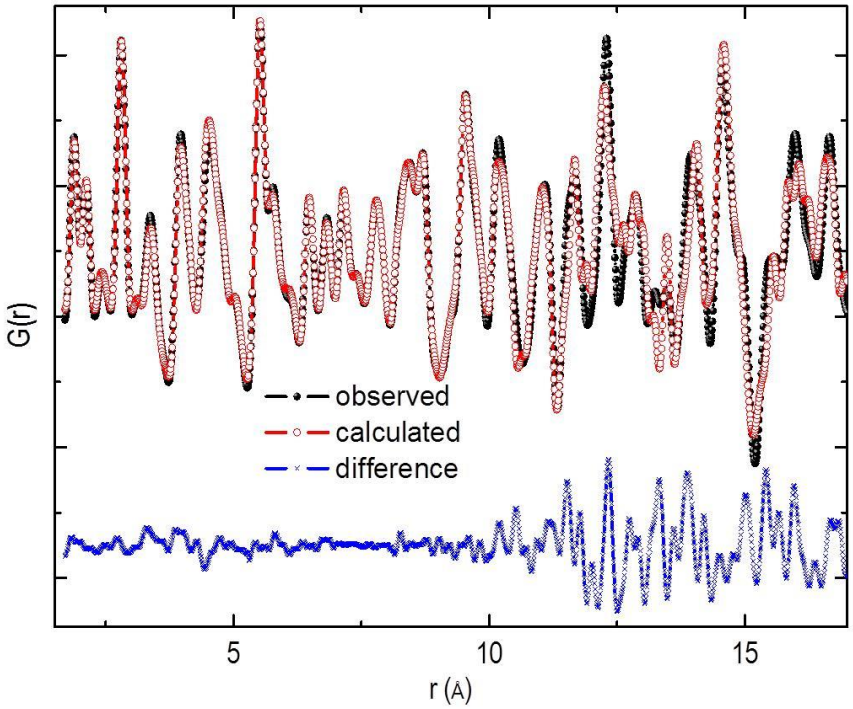

Figure 15. Local structure fitting of $NaNbO_3$ at 15K
Neutron pair distribution function $G(r)$ analysis of $NaNbO_3$ at 15K with only the *R3c* group. Note that the differences are very small below 10 Å and begin to become obvious above 10 Å.

Pair distribution function analysis at low temperatures

When $NaNbO_3$ is cooled down below room temperature, it exhibits ferroelectric behaviors due to the spontaneous polarization formed in its structure. A great deal of research has been focused on the structure in this range of temperature, and it is generally agreed that two phases, *R3c* and *Pbcm*, coexist. Our Rietveld analysis also shows the coexistence of the two phases. Two-phase coexistence in a compound at low temperatures usually signifies that at least one of the phases is metastable. The PDF analysis explained why this occurred.

As shown in Figure 14, if we use the model obtained from the Rietveld refinement, the PDF fitting confirms the two phase coexistence at r > 10 Å. However, it is clearly shown in Figure 15 that below 10 Å, *R3c* is the only phase group that correctly describes the local atomic distribution. Additionally, largest off-centering displacements of Na atoms and the most significant distortions in Na-O-Na correlations are indicated (similar to that shown in Figure 11), which is the result of the flexibility of Na atomic position. The radius of sodium ion is very small (1.02 Å),[46] whereas it is surrounded by 12 nearest oxygen atoms (1.40 Å in radius[46]) with the average Na-O distance of 2.79 Å. These oxygen atoms form a cage with very large space for a Na atom to move around. Of course, Nb atoms also have off-centered displacement, as believed conventionally. But

the nominal ionic size of Nb (0.74 Å)[46] is much larger for the volume of the octahedron formed by the six oxygen atoms surrounding Nb. Thus the picture of Nb rattling in the O_6 cage is invalid.

Below 190 K, $NaNbO_3$ falls in the ferroelectric state, with the parallel spontaneous polarization. Again, if we compare the PDF in the very short range (three red lines in Figure 12), namely within the size of the elemental perovskite unit cell, the splitting of the first peak confirms the Nb-O variations in the NbO_6 octahedra, one at r = 1.87 Å and the other at r = 2.1 Å, which is attributed to the off-centered displacement of Nb atom. Especially, the two Nb-O peaks are not identical and the ratio of their intensities is about 1.5. In some previous studies, Nb was considered tomove towards the [111] direction of the NbO_6. But in such a case the split Nb-O peaks should have the 1:1 intensity ratio. Our PDF result seems to indicate that Nb moves towards a direction between (111) and (110). Moreover, with the evolution of temperature below 190K, the peaks of Nb-O bond lengths prefer to stay the same, but the Na-O bond correlation peak shifts very significantly. During cooling, the amplitude of thermal vibration of Na becomes very small, which leaves Na to more clearly off-centered positions. At 15K, two well-defined Na-O peaks are formed at r = 2.4 and 3.1 Å, inferring that Na atoms have about 14% off-centering from the center of the oxygen cage, much larger than the off-centering of Nb atoms. Also, the ratio of the intensities of these two peaks is again about 1.5, though the intensities are relatively small due to broadening of average Na-O correlations. That means Na may have a similar direction of movement as Nb. The coincidence of Na and Nb off-center displacements contribute to the formation of large dielectric polarization.

From 490 to 300 K, the space group at short range is always *R3c*, which is a ferroelectric (FE) state. However, the structure over the long distance beyond 10 Å is always antiferroelectric (AFE) with the *Pbcm* group symmetry. This can only mean that nanoscale twins are formed in the *R3c* phase with the ferroelectric polarization changing from one twin to another. Above room temperature, this kind of average AFE structure appears through the whole lattice. Below 190 K, some of the FE domains are larger, while much of the FE domains remain in the nanoscale twins, resulting in apparent coexistence of the *R3c* and *Pbcm* phases.

The results of PDF fitting clearly indicate that the true ground state for the local structure of $NaNbO_3$ below 490 K is actually the *R3c* structure. It is the real phase of $NaNbO_3$ at low temperatures, but they tend to form nanotwins, resulting in the appearance of the *Pbcm* phase at long ranges. It should be noted that if the twins are regularly spaced they should result in superlattice diffraction, and a different structure with a large unit cell. That such superlattice diffraction peaks are not observed implies the spacings of nanotwins are irregular. As noted by Hendrick and Teller[47] for partially ordered layered lattices of graphite, such irregular, random arrangement of twins can produce sharp diffraction peaks with the average lattice structure, in this case *Pbcm*, rather than broad diffraction patterns corresponding to the short structural coherence length.

The most probable cause of the formation of nanotwins is the low mobility of Na ions at low temperatures. The off-centering of Na is quite large, as much as 0.4 Å, greatly

contributing to large ferroelectric polarization. But at the same time the energy barrier to move from one off-centered position to another must be significant, resulting in trapping of Na ion in one of these off-centered positions at low temperatures. This makes formation of large FE domains difficult, resulting in nanotwin states. The large barrier for motion also explains the hysteric effect naturally without invoking the idea of quantum paraelectricity.[48] On the other hand, as we mentioned earlier, replacing Na with other elements such as K can improve its ferroelectric and piezoresponse performance. The ionic radius of K^+ is larger than that of Na^+ by 0.25 Å,[46] reducing the off-centering to only 0.1 Å. The energy barrier for such a small off-centering is negligible, making K^+ much more mobile than Na^+, although the contribution of K+ to ferroelectricity is smaller. Apparently, the new lead-free ferroelectric materials[27] were synthesized by improving the mobility of alkali ion at the expense of losing some polarization, by partially replacing Na by K.

Conclusions

In summary, we have discovered the local aspect of evolution of the structure and space group of sodium niobate from 930 K down to 15 K through the combination of the standard neutron scattering diffraction Rietveld analysis and the local pair distribution function (PDF) study. The long range crystallographic phase undergoes six phase transitions, through cubic, tetragonal, orthorhombic, and rhombohedral. However, the study of the short-range structure demonstrates that in spite of such complexity there are only three main patterns in the local structures, as shown in Figure 12. At high temperatures (above 490 K), local dielectric polarization is absent. In the intermediate temperature range (down to 300 K), Nb starts to become off-centered, but Na remains centered. Only below 300 K, both Nb and Na become off-centered. The study of the local structure brought further new information. Especially at low temperatures, where $NaNbO_3$ experiences antiferroelectric and ferroelectric transitions, our local PDF shows that the short-distance structure is always in the *R3c* space group, which is actually the real ground state. In the long range, however, the nanotwined structure of the *R3c* cells brings the appearance of the *Pbcm* space group. Our discovery solves the long-standing controversies in numerous neutron studies of sodium niobate at low temperature and explains why $NaNbO_3$ is a good base compound for promising new ferroelectric materials that can substitute lead-containing toxicant materials.

CHAPTER III
FERROELECTRICS/MANGANITES HETEROSTRUCTURES

After the discussion and elucidation of the physical origin and lattice structure of ferroelectric oxides in the last chapter, the application of the switchable polarization of ferroelectrics follows. Effective ferroelectric control of some functional oxides can lead to remarkable physical phenomena. We move on to the field effect study in ferroelectric and ferromagnetic heterostructures in both in-plane and out-of-plane directions in this chapter.

Strongly coupled phase transition in ferroelectric/correlated electron oxides heterostructures

Introduction

Sr-doped $LaMnO_3$ ($La_{1-x}Sr_xMnO_3$, LSMO) has a rich phase diagram and exhibits a wide spectrum of magnetic and electronic properties, mainly due to the strong coupling among spin, charge, orbital, and lattice degrees of freedom.[49–51] The phase diagram of LSMO reveals numerous different phases with increasing x (hole doping), as partially shown in Figure 16(a): spin-canted insulator (C-I), ferromagnetic insulator (FM-I), ferromagnetic metal (FM-M), and antiferromagnetic insulator (AF-I). The complicated phase diagram manifests the material's sensitivity to external stimuli, such as thickness,[52–56] strain,[57–59] microstructure, and lattice distortion,[60] in addition to chemical doping and temperature. In particular, in the vicinity of its phase boundaries, for instance x=~0.2, the phase of LSMO is most susceptible to a small perturbation and, thus, even an insulator-metal transition (IMT) can be realized in controllable fashion.

As one of the controlling parameters, electric polarization in ferroelectrics can be efficiently used to tune the characteristics of LSMO. In oxide heterostructures, it has been frequently shown that the physical property of LSMO could be manipulated by the neighboring ferroelectric layer.[61–65] Even though the concept of ferroelectric field effect seems promising, the direct probing of the field-induced change in electronic and magnetic ground states with a conventional capacitor as a function of the polarization direction has been rather limited due mainly to the following reason: It is practically impossible to switch the polarization across a large area of a macroscopic ferroelectric layer (typically several mm^2) needed for DC transport and magnetic measurements, since the required energy to switch the polarization is extremely high. Even if one could reach the required energy level, the typical size of the top electrode should be relatively small (in the order of 100 lm in diameter or less). Otherwise, when a larger capacitor is used, a huge charging current due to a large RC time constant would hinder the reliable ferroelectric switching. In addition, it is almost impossible to avoid unwanted pinholes or particulates in thin films prepared by most physical vapor depositions. To overcome this

problem, some studies used sub-micron-size field effect transistor and observed ferroelectric switching dependent changes in the manganite layer in ferroelectric/manganite heterostructures.[66] However, a clear IMT has not yet been achieved with the ferroelectric polarization control, most probably due to additional sample processes including nanolithography, which induces more complications to the system. The absence of the experimental data hampered the understanding of the detailed mechanisms for ferroelectric field effect. It is worthy of note that there have been attempts to switch the polarization of the whole layer by using ambient gas[67] or mechanical pressure,[68] but the LSMO phase change using ferroelectric switching has been rarely explored in such cases.

In this letter, we show that IMT can be realized in LSMO by capping the layer with a ferroelectric PZT epitaxial layer. Correspondingly, the ferromagnetic phase transition temperature (T_C) and saturation magnetic moment (M_s) were also substantially tuned depending on the doping level, indicating a clear crossover across the phase boundary of LSMO by ferroelectric field effect. Comparison with nonferroelectric $SrTiO_3$ (STO) and $LaAlO_3$ (LAO) capping layers excluded other possible origins for the IMT in the LSMO layer, besides ferroelectricity.

Measurements

A group of LSMO (with nominal x=0.2) heterostructures were epitaxially fabricated by pulsed laser epitaxy on atomically smooth TiO_2-terminated (001) STO substrates. The thickness of the LSMO layer was varied as 5, 10, and 30 nm. We then deposited 10-nm-thick PZT, STO, and LAO ultrathin films as capping layers on top of the LSMO layers. The samples were fabricated at 625°C in 100 mTorr of oxygen partial pressure. A KrF excimer laser (λ=248 nm) with a laser fluence of ~1J/cm^2 was used for ablating sintered PZT and LSMO targets and single crystal STO and LAO targets. Typical polarizations of our PZT thin films were ~80μC/cm^2, with not much thickness dependent fluctuations. Details on the growth condition can be found elsewhere.[69]

Figure 16(a) shows a schematic diagram of our samples. The topography of a final PZT/LSMO heterostructure was observed by atomic force microscopy (AFM), showing an atomically flat surface and well-defined terraces, as shown in Figure 16(b). Note that the growth of atomically flat, high quality heterostructures is a critical step towards obtaining the high polarization in PZT, required for effective ferroelectric switching with an ultrathin film.[69] Also note that the image is after positive and negative ferroelectric switching, which indicates that the surface topography is not influenced by the ferroelectric poling. The phase images of the PZT film with LSMO as a bottom electrode were measured by piezoresponse force microscopy (PFM) as shown in Figure 16(c). The polarization was switched by a conductive AFM tip using +2.5 and -2.5 V. The PFM image of the PZT film reveals that it has a single as grown ferroelectric domain with an upward polarization direction and clear ferroelectric switching property. On the other hand, the PFM images from the LAO/LSMO (Figure 16(d)) and STO/LSMO (data not shown) heterostructures, which we have grown to validate the ferroelectric field effect,

indicate that both LAO and STO layers are indeed non-ferroelectric. Temperature (T)-dependent resistivity curves, ρ(T), were recorded by a physical property measurement system (PPMS, Quantum Design Inc.). Ohmic indium contacts were ultrasonically soldered to the samples' corners in van der Pauw geometry and, then, gold wires were bonded to the contacts as schematically shown in Figure 16(a). T and magnetic field dependent magnetization curves, M(T) at 200 Oe and M(H) at 10K, were recorded using a 7 T superconducting quantum interference device (SQUID, Quantum Design Inc.) magnetometer.

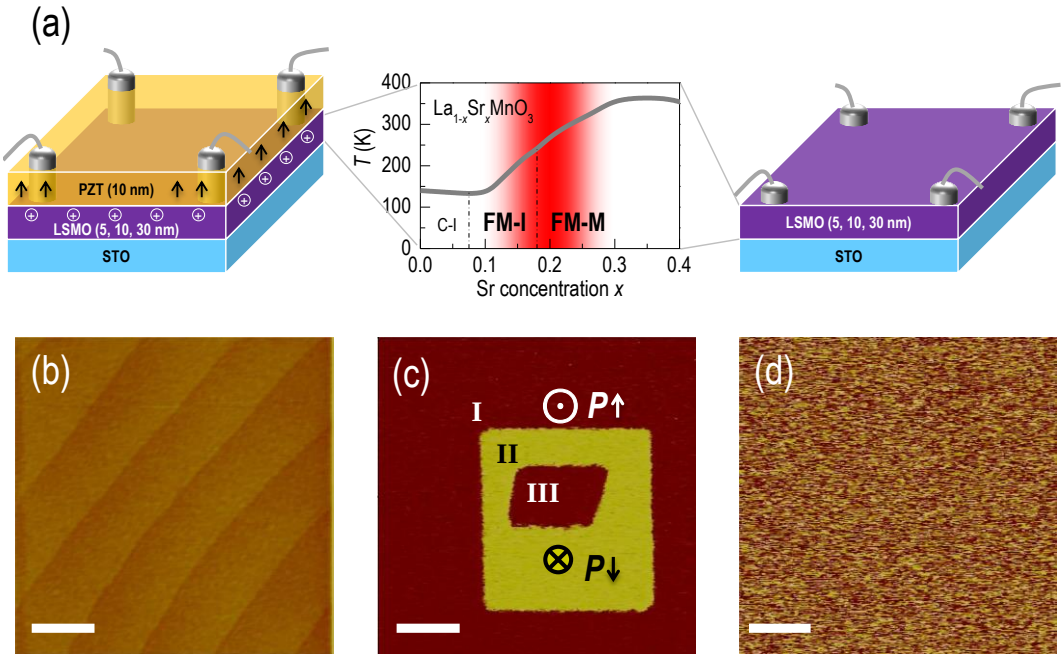

Figure 16. Schematics and surface condition of manganites films and heterostructures

(a) Left and right images represent schematic drawings on a PZT/LSMO heterostructure and a LSMO thin film on STO, respectively. The electrodes for in-plane van der Pauw transport measurements were contacted to the LSMO layer. The image in the middle shows a part of the phase diagram of $La_{1-x}Sr_xMnO_3$. (b) Topographic image of a PZT(10 nm)/LSMO(5 nm) heterostructure deposited on a (001) STO substrate, showing an atomically smooth surface with clear step-terrace structure. (c) PFM image of PZT on bottom electrode LSMO showing clear ferroelectric switching in the PZT layer. The contrast was produced by a conductive AFM tip under +2.5V and -2.5 V, for downward (⊗) and upward (⊙) domains, respectively. Region I correspond to as-grown background, and Regions II and III correspond to positively and negatively poled regions, respectively. (d) PFM image of a LAO on LSMO showing no piezoresponse. The scale bars on the images correspond to 400 nm.

Results and Discussions

When more holes are doped into LSMO (i.e., x is increased) near x=0.2 across the phase boundary, we can expect two different phenomena as illustrated in Figure 16(a): The system will undergo an IMT and the magnetic T_C will increase with increasing x. Figure 17 demonstrates that by observing these two phenomena, we could successfully control the phase of LSMO not through chemically adding extra holes, but by electrostatically using a ferroelectric capping layer. As shown in Figure. 17(a), the bare LSMO film exhibited a highly insulating ρ(T) behavior with a T_C of ~200K (marked with a triangle). On the other hand, the PZT/LSMO heterostructure exhibited a metallic ρ(T) behavior over a wide range of T. Surprisingly, ρ(T) was decreased by at least four orders of magnitude at ~70K by capping with the PZT layer. This ratio seems to be further increased at lower T (the bare LSMO's resistivity at lower T was above the instrumental limit.) The T_C was also increased substantially to~250 K, as expected from the field doping. The increase in ferromagnetic T_C by the ferroelectric layer was confirmed by the M(T) curves as shown in Figure 17(b). Furthermore, an evident increase in Ms in the LSMO layer, from 2.06 to 3.71 μ_B/Mn, was observed with PZT capping, as shown in the M(H) curves in the inset of Figure 17(b).

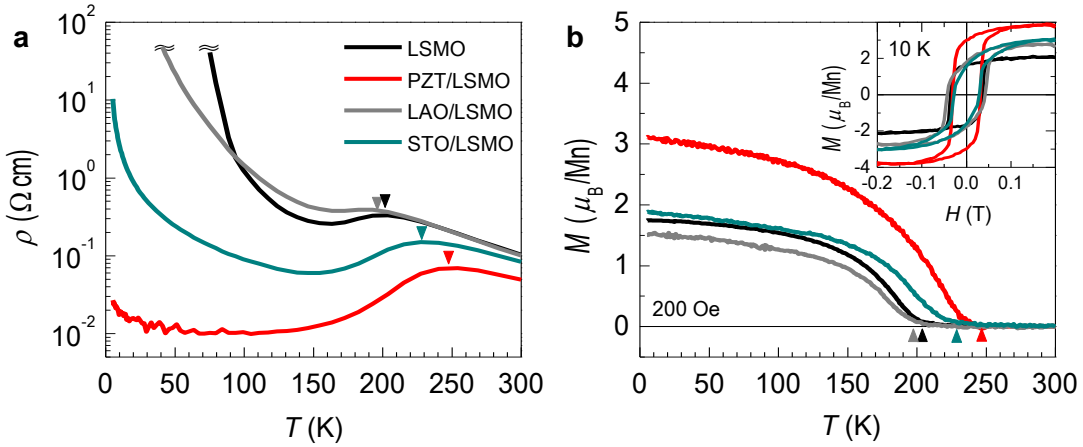

Figure 17. Electronic and magnetic properties of various ferroelectric heterostructures

Transport and magnetic properties of ultrathin (5 nm) LSMO films with different capping layers of PZT, STO, and LAO. T_c is marked with a triangle. (a) Temperature-dependent resistivity for LSMO with 10 nm capping layers. (b) Temperature-dependent magnetization of LSMO and LSMO with 10 nm capping layers thereon measured at 200 Oe. Inset shows magnetic hysteresis loops for corresponding samples measured at 10K.

It is obvious that the boundary condition of LSMO changes with ferroelectric capping, and this strongly affects the physical properties of the layer. In particular, the upward ferroelectric polarization of the as-grown PZT layer (see Figure 16(c)) will attract more holes to the PZT/LSMO interface. Consequently, the carriers will be accumulated near the interface to screen the electric field, as schematically shown in Figure 16(a). The

increased hole density would increase the conductivity of the LSMO layer, eventually crossing the insulator-metal phase boundary. There can be an alternative picture, which does not necessarily contradict with the previous scenario. Note that both FM-I and FM-M phase domains coexist for LSMO near x=~0.2.[70,71] The hole accumulation due to the ferroelectric field effect would enhance the population and/or size of the FM-M phase domains, bringing the system above the percolation limit to exhibit the metallic behavior. The increased T_C evidently supports this idea, because the increased magnetic double exchange interaction results in the increased fraction of FM-M phase domains.

In order to confirm that the large change in the physical properties of the LSMO layer is actually resulting from the ferroelectric layer, we deposited non-ferroelectric capping layers (STO and LAO) instead of PZT. As shown in Figure 17, ρ(T), M(T), and M(H) curves of LAO/LSMO are very similar to those of bare LSMO with no capping layer. This clearly illustrates that a non-ferroelectric layer does not change the electrostatic boundary condition in LSMO as compared to air (i.e., non-capping situation). On the other hand, the results on the STO/LSMO heterostructure deviated slightly from the bare LSMO, although the change was weaker than that for PZT/LSMO. While more detailed study is required to exactly determine the role of STO capping layer, we suggest a charge transfer across the interface as one of the origins of the change in the physical properties in STO/LSMO. In particular, STO is known to easily supply oxygen to the LSMO surface that possibly has an oxygen deficient dead layer.[72,73] Thus, the changes in ρ(T) and TC in STO/LSMO might be related with the fact that some of oxygen defects in LSMO were compensated by interfacing with STO. In addition, cation intermixing or doping to the interface between the LSMO and STO might also be possible. However, it is unlikely based on our atomically flat topography and well-defined x-ray reflectivity fringes, indicating a rather sharp interface.

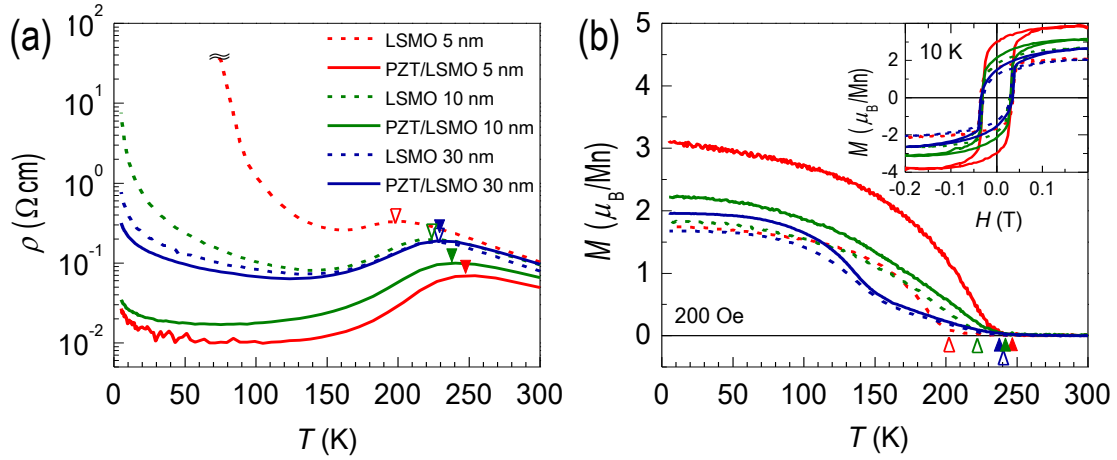

Figure 18. Thickness dependent electronic and magnetic properties of PZT/LSMO

LSMO thickness dependent transport and magnetic properties of LSMO films with 10 nm-thick PZT capping layers. T_c for LSMO/STO and PZT/LSMO/STO heterostructures are marked with empty and solid triangles, respectively. Temperature-dependent (a) resistivity and (b) magnetization for 5, 10, and 30 nm LSMO with and without PZT

capping layers. Inset shows the magnetic hysteresis loops for corresponding samples measured at 10 K.

We further studied the dependence of the ferroelectric field effect on the thickness of LSMO. If the ferroelectric PZT layer has the largest influence near the PZT/LSMO interface, the effect will decrease as the LSMO thickness increases. Figure 18(a) shows ρ(T) of 5, 10, and 30 nm of LSMO with and without a PZT capping layer. It certainly shows that the change coming from the PZT capping decreases as LSMO thickness increases. For bare LSMO, the resistivity was increased with decreasing thickness. When the thickness of the LSMO layer was smaller than 10 nm, i.e., for 5 nm LSMO, the film became highly insulating, suggesting that the critical thickness for the metallic LSMO is between 5 and 10 nm. A similar thickness dependent transport behavior has been reported for LSMO with x=0.3 thin films,[51] where they suggested a loss of a conducting percolation path for LSMO layers thinner than ~3.2 nm. Those x=0.3 LSMO films have more stable FM-M phases compared to the case of x=0.2 reported here, which could explain the difference in the critical thicknesses. However, the same argument can be applied for the x=0.2 LSMO films. When these LSMO films are capped

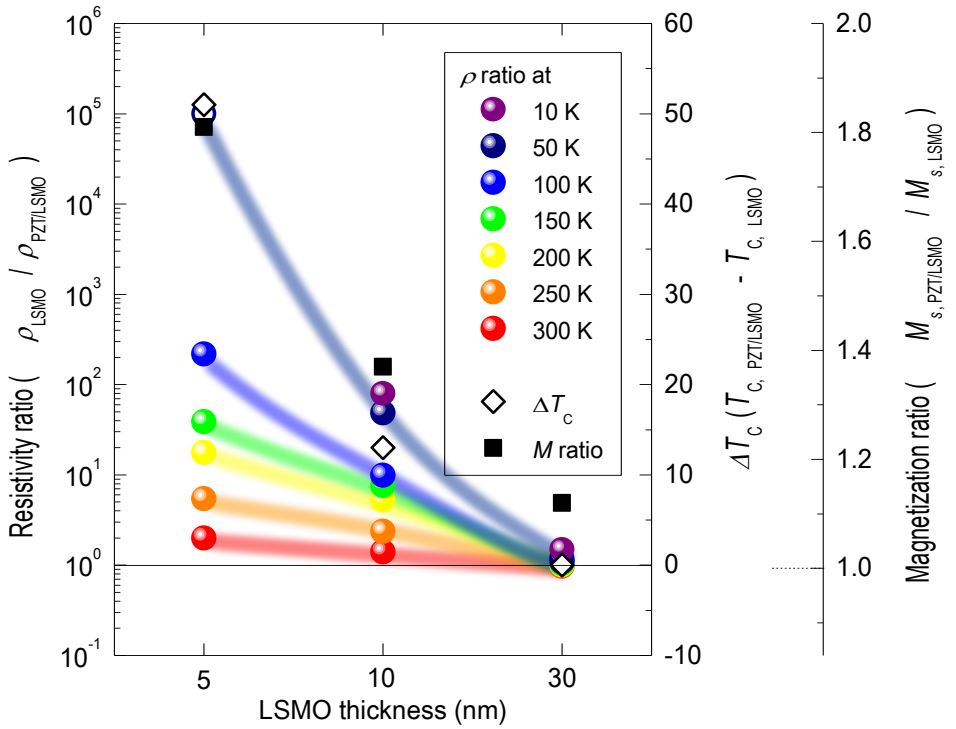

Figure 19. Summary of resistivity ratio of PZT/LSMO and LSMO films

ρ(T) ratio, ΔT_C, and Ms ratio at 10K at 0.2 T between LSMO and PZT/LSMO, for different LSMO thicknesses. The value for the open circle symbol in dark blue (50 K) was estimated from extrapolation by fitting the resistivity curves with the Arrhenius function. The thick solid lines are guide to the eye.

with PZT, ρ(T) decreases regardless of the LSMO thickness. However, the effect was the largest for the 5 nm LSMO film, the thinnest among studied here. While other contributions such as compensation of surface dead layer and/or prevention of carrier depletion due to capping layer might also play some role, it is evident that the ferroelectric field effect is the largest near the interface of PZT/LSMO interface with the thickness of several nanometers. Figure 18(b) shows the magnetic properties of the samples. It shows an increase in T_C and M_s with PZT capping, but again, the amount of change decreases with increasing LSMO thickness. We note that M(T) curves for 30 nm LSMO with and without the PZT capping layer are different from others, i.e., it seems to show two different transitions with decreasing T. While it requires a detailed study on the magnetic property, we suggest that the strain relaxation leading to some lattice distortion in the thicker film might be attributed to such an exotic behavior.

Figure 19 summarizes the transport and magnetic properties of LSMO and PZT/LSMO heterostructures, as a function of the LSMO thickness. The resistivity ratio between PZT/LSMO heterostructure ($\rho_{PZT/LSMO}$) and LSMO film (ρ_{LSMO}) clearly increased as T decreased. As expected, the resistivity ratio of the 5 nm-thick LSMO increased most rapidly. Surprisingly, at 50 K, we could obtain a resistivity ratio greater than five orders of magnitude, by extrapolating the ρ(T) for the bare 5 nm LSMO. The extrapolation was done by fitting the curve using the Arrhenius function, which could fit other insulating curves (10 and 30 nm) of LSMO at low temperature quite well. Figure 19 also shows the change in T_C ($\Delta T_{C,}=T_{C,PZT/LSMO}-T_{C,LSMO}$) between PZT/LSMO and LSMO, for different LSMO thicknesses. For 5 nm-thick LSMO, the change in T_C due to ferroelectric capping is increased by ~50 K. Finally, Ms ratio at 10 K, at 0.2 T between PZT/LSMO and LSMO ($M_{s,PZT/LSMO}/M_{s,LSMO}$) is shown. The strongest effect of ferroelectric layer is again shown from the thinnest LSMO film, enhancing Ms as large as twice. These results clearly indicate that the phase of LSMO is most susceptible to the ferroelectric polarization near the interface of PZT/LSMO.

Conclusions

In summary, substantial changes in transport and magnetic property of LSMO ultrathin films under the influence of ferroelectric polarization have been reported. As compared to the bare LSMO thin films, PZT/LSMO heterostructures showed a large modulation of resistivity, magnetic phase transition temperature, and saturation magnetization. Moreover, we have confirmed that an insulator-metal transition transition in manganites can be achieved when the manganite layer is sufficiently thin as the field effect is dominantly active near the interface, driven by ferroelectric polarization. Therefore, our unambiguous observations on the ferroelectric field effect control could aid understanding and controlling functional oxide heterostructures, opening a door to realizing oxide electronic devices such as ferroelectric field effect transistors and non-volatile data storage.

Tunneling Electroresistance Induced by Interfacial Phase Transitions in Ultrathin Oxide Heterostructures

Introduction

In quantum electronics, an ultrathin insulating layer sandwiched by two metallic electrodes serves as a tunnel junction (TJ), where electrons pass through the barrier by the quantum tunneling process. Depending on the selection of electrode materials, a wide range of TJs can be designed and utilized for various purposes. For example, semiconductor tunnel diodes are used for amplifiers and frequency converters,[74] magnetic TJs for magnetic detectors in hard disks,[75] and superconducting TJs utilizing the Josephson effect for magnetometer applications.[76] Recently, an upsurge of interest has focused on electrically-induced large resistance changes by using TJs with ferroelectric (FE) insulating barriers, displaying the so-called tunneling electroresistance (TER) effect (see Figure 20a).[77,78] The spontaneous polarization of the FE barrier is predicted to affect the tunneling behavior in FE tunnel junctions (FTJs) through the

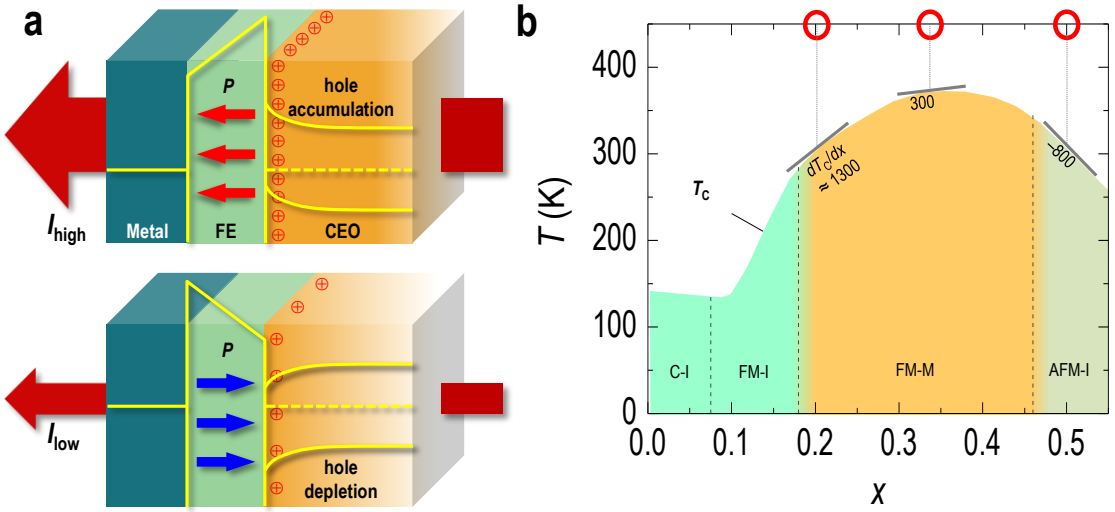

Figure 20. Interfacial phase modulation by FE.

(a) Schematic representation of Metal/FE/CEO TJs. Energy band diagrams of FTJs at zero external bias are also drawn for two polarization directions. The carrier population is controlled by the direction of the polarization, which yields either hole accumulated (top) or depleted (bottom) state in the CEO layer. (b) Phase diagram of bulk LSMO varying x [Ref. 91]. Near $x \sim 0.20$, T_C changes the most with x ($dT_C/dx \sim 1300$), near $x \sim 0.50$ the change is less drastic ($dT_C/dx \sim -800$), and near $x \sim 0.33$ it is the smallest ($dT_C/dx \sim 300$).

interface effect,[79] inverse piezoelectric response,[80,81] and modification of the band structure of the FE barrier,[82] resulting in a bi-stable state for non-volatile switching. Correlation between the FE polarization orientation and the tunneling conductance due to the change of electrostatic potential across the FE layer has also been observed in FE oxide heterostructures.[77,83-86] This FE field induced modulation of the TER can be particularly interesting when the FE layer is combined with correlated electron oxides (CEOs) as the metallic electrodes. Up to now, however, the role of the metallic electrode (the CEO layer in the heterostructure) has often been ignored or underestimated in explaining the TER effect. While an electronic phase modification in the electrode by a neighboring FE layer has been theoretically predicted in seminal work by Tsymbal and collaborators,[77,87] there have been only few experimental efforts to attest those predictions.[88,89] This is largely due to the absence of a direct FE control on both the electronic and magnetic states of the CEO layer, even though electric-field controlled modifications of the magnetism or magnetic-field dependent resistivity changes have been observed in oxide heterostructures.[90] Since the modification of the CEO state should naturally accompany drastic changes in the physical properties of the heterostructures, this approach encompasses great potential for novel device applications, which could effectively utilize CEO phase modifications by controlling the FE polarization (Figure 20a).

$La_{1-x}Sr_xMnO_3$ (LSMO) is a hole-doped CEO and an excellent model system to explore the above-described effects because its electronic and magnetic phases are highly susceptible to a small change in doping (Figure 20b).[91] Therefore, a strongly coupled phase modulation could significantly influence the TER magnitude. An ultrathin LSMO was chosen as the CEO layer to maximize the effect and to convincingly confirm the expected effects by investigating both its electronic and magnetic properties. We note that, while LSMO thin films have been frequently used as bottom electrodes in FTJs in some previous studies, its contribution to the junction transport has never been fully appreciated.[83,85,92,93] In this work, we systematically investigate the coupled phase modulation in the oxide heterostructure by varying the nominal composition x in LSMO (x = 0.20, 0.33 and 0.50). $PbZr_{0.2}Ti_{0.8}O_3$ (PZT) has been chosen as the FE layer owing to its large remnant polarization (typically, our highly polar PZT film has a remnant polarization, P_r = ~80 μC/cm^2, without much thickness dependent variations.).[94] It is also worth noting that a large polarization is indispensable to strengthening the coupling across the heterointerface without the dielectric breakdown typically found in non-FE-containing field effect devices.[94] Schematics of heterostructures and corresponding energy band diagrams are shown in Figure 20a to illustrate the main ideas. When the FE polarization is upward, the carriers (holes) in LSMO become accumulated due to the spontaneous electric field at the interface. Conversely, when the polarization is downward, a hole-depleted state is realized. In addition to the different shape of the PZT band due to the polarization reversal, the hole depleted/accumulated-state yield a substantial change in the in-plane and out-of-plane transport properties in FTJs. Even more importantly, the hole depletion/accumulation could trigger the crossing of a phase boundary of LSMO (Figure 20b), providing us with another degree of freedom which could largely amplify or even reverse the TER effect.

Measurements

All samples were *in-situ* grown by pulsed laser epitaxy on atomically smooth TiO_2-terminated $SrTiO_3$ substrates at 625 °C in 100 mTorr of oxygen. The growth at the high pressure oxygen partial pressure ensures the quality of our ultrathin heterostructures with chemically abrupt interfaces,[107] as confirmed by Z-contrast scanning transmission electron microscopy. A KrF excimer laser (λ = 248 nm) with a laser fluence of ~1 J/cm^2 was used for ablating sintered PZT and LSMO targets. Details on the growth condition can be found elsewhere.[94]

A combination of nanoscale polarization and local conductance were mapped by PFM and CAFM. Clear FE response of hysteretic piezoresponse and switching behavior were observed with a single as grown FE with an upward polarization direction. $\rho(T)$ curves were recorded by a 14 T physical property measurement system (PPMS, Quantum Design Inc.). Ohmic indium contacts were ultrasonically soldered to the samples' corners in Van der Pauw geometry and, then, gold wires were bonded to the contacts. $M(T)$ curves at 200 Oe were recorded using a 7 T superconducting quantum interference device (SQUID, Quantum Design Inc.) magnetometer. The structural quality of the heterostructures was investigated by x-ray diffraction and scanning transmission electron microscopy. For the later, we used the state-of-the-art JEOL ARM 200 CF, which was equipped with two aberration correctors (CEOS) and a cold field-emission gun, routinely achieving a spatial resolution of 0.8 Å. The range of collection angle of 68 to 280 mrad was used for high-angle annular dark-field imaging.

The model calculations were done using a 4×4×12 lattice with twisted boundary conditions (TBC) in plane, and open boundary conditions (OBC) perpendicular to the film. In order to eliminate the surface termination effect on the ferroelectric switching, a mixed surface termination (50%) of LSMO has been used for the calculations. The TBC, with a 6×6 k-mesh, can reduce finite size effects.[108] Several dielectric constants from 20 to 180 were used and all give qualitatively similar results, although the screening length depends on the dielectric constant value. With regards to the t_{2g} spins, a FM background for x = 0.20 and 0.33 and an A-AFM background for x = 0.50 were adopted to calculate the electronic distribution (Figure 24).[95] To account for the interfacial phase transitions, the system energies are compared between the original spin t_{2g} backgrounds and those obtained by switching the background to the competing state, as done in Refs. 78 and 79. For example, in the x = 0.50 case with FE polarization pointing to the LSMO, four interfacial LSMO layers become FM when using $J_{AFM} = 0.1t_0$, where J_{AFM} is the superexchange coefficient and t_0 is the DE energy unit (~0.5 eV).[91,103] Note that, in Figure 24, the changes in the hole density can be very large particularly for the first layer in our idealized calculation. However, our results should be considered only an upper bound on the density modifications that can be achieved by the influence of the FE component. In particular, issues such as the lattice distortions in the vicinity of

the interface have not been considered in our effort. For more details the reader should consult Ref. 30.

Results and Discussions

The impact of the FE polarization on the electronic and magnetic state of the LSMO layer could be clearly observed from the in-plane transport and magnetic properties of our heterostructures, as summarized in Figure 21. Since it was impossible to switch the as-grown polarization on the macroscopic scale necessary for the in-plane measurements, we compared the results of various LSMO ultrathin films with (upward polarization) and without (no polarization) a PZT capping layer. As previously reported, the spatial extent of the ample FE polarization effect is limited to only a few nanometers.[96] Therefore, we focused on heterostructures with an ultrathin LSMO layer (5 nm). The polarization direction of the as-grown PZT was upward, so the LSMO film with PZT capping layer should have a hole accumulation state. This would shift the LSMO phase to the increased doping side, *i.e.* to the right in Figure 20b. The temperature dependent resistivity, $\rho(T)$, curves in Figure 21a shows that x = 0.20 LSMO indeed exhibits a remarkable polarization-induced insulator-to-metal transition. In the case of the PZT/LSMO heterostructure, the drastically reduced $\rho(T)$ value, the increased ferromagnetic (FM) Curie temperature (T_C), and the increased magnetization coherently indicate the modification of the electronic and magnetic state of LSMO from a FM insulator to a FM metal by the FE polarization. Note that the strong FE field effect control, yielding here, *e.g.* a 100,000 fold change in resistivity at 50 K, is solely related with the polarization of our PZT film.[96] Such a huge change in resistivity by FE polarization is amongst the largest ever reported.[88] On the other hand, Figure 21c

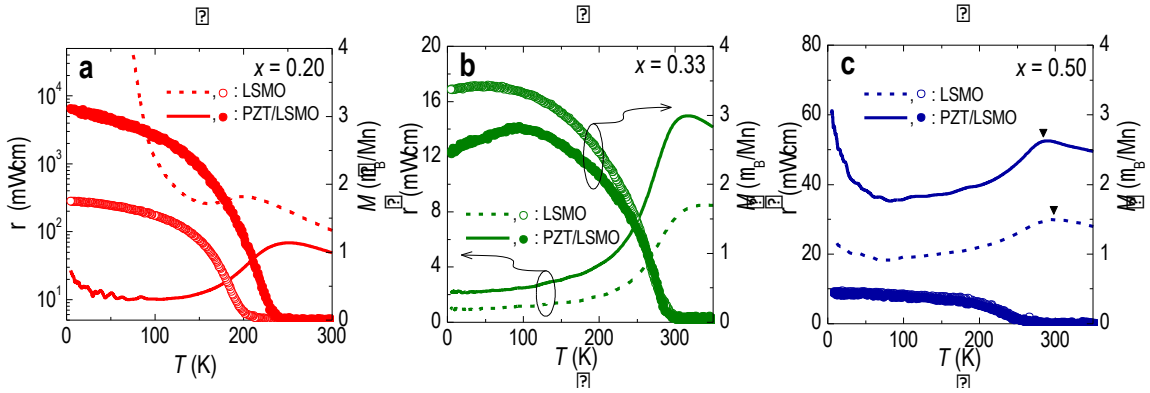

Figure 21. FE control of in-plane transport and magnetic properties.

In-plane resistivity (ρ) (lines) and magnetization (M) (symbols) as a function of T. Results for ultrathin LSMO with compositions (a) x = 0.20, (b) 0.33, and (c) 0.50 are shown with and without PZT capping layers. Note that (a) is reproduced from Ref. 71.

shows results for x = 0.50 LSMO displaying an opposite trend to that of x = 0.20 LSMO: $\rho(T)$ now increases with the FE field induced doping. While it was rather difficult to determine T_C from the suppressed temperature dependent magnetization $M(T)$ curves due to the antiferromagnetic (AFM) phase of the highly doped LSMO, the T_C estimation from the peak in the $\rho(T)$ curves (denoted as triangles) shows a slight decrease in T_C with the PZT layer on top of the LSMO layer. Note that the suppressed changes in T_C compared to those of x = 0.20 LSMO might be due to the reduced slope value of the x-dependent T_C curve, as shown in Figure 20b: the slope near x = 0.50 (~ –800) is only about 60% of the value near x = 0.20 (~1300). Based on the results for x = 0.20 and 0.50 LSMO, it can be further expected that x = 0.33 LSMO should display less pronounced changes than the other compositions in the electronic and magnetic properties by the FE field induced doping. Indeed, as shown in Figure 21b, the changes in $\rho(T)$ due to the PZT capping are weaker when compared to the heterostructures with x = 0.20 and 0.50 LSMO. The overall changes in the in-plane physical properties clearly indicate that the FE field doping is an efficient way to controlling the phase of the CEO layer,[63] which could substantially influence on the TER effect in the oxide heterostructure, as discussed later.

Figure 22 shows the polarization direction dependent tunnel currents, or TERs in a PZT/LSMO (x = 0.20) heterostructure. Figure 22a shows a piezoresponse force microscopy (PFM) phase image of the sample at room temperature, which was poled with an incrementally increasing *dc* poling bias. The gradual change in the applied voltage used in switching the polarization direction shows that the coercive voltage is ~2 V. The conducting atomic force microscopy (CAFM) image for the corresponding area is shown in Figure 22b. The current map was collected at a tip bias voltage (–1.5 V). A distinct contrast has been observed in the current map, where the upward FE polarization of PZT leads to a significantly higher current. While a portion of the CAFM image includes noisy current spots due to instrumental limitations (see Supporting Information for more detail), the clear correlation between the PFM phase and CAFM images serves as a convincing proof that the FE polarization plays an important role in determining the tunneling current through the heterostructure.[83,84]

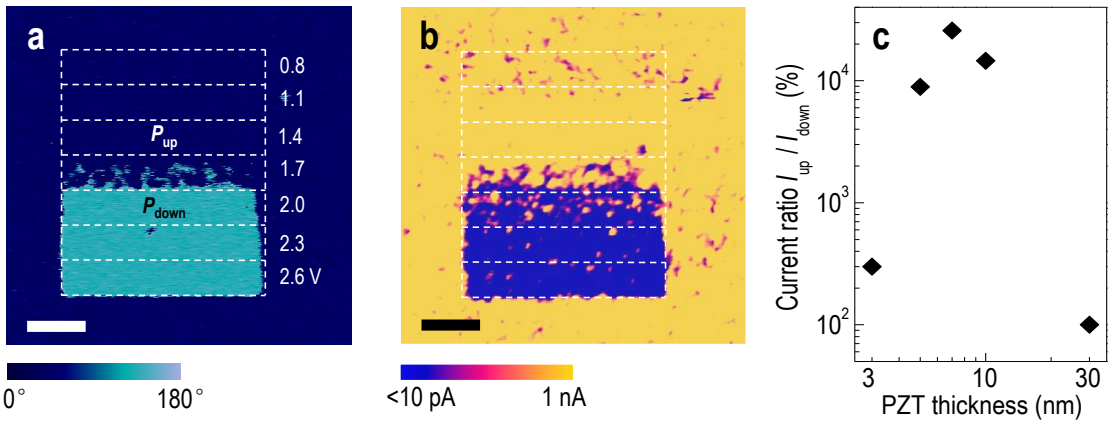

Figure 22. Polarization direction dependent tunneling.

(a) Voltage-dependent PFM phase image of a PZT/LSMO (x = 0.20) heterostructure at room temperature. The thicknesses of PZT and LSMO were 10 and 5 nm, respectively. (b) CAFM map for the area corresponding to (a). Upward polarization results in higher current. In (a) and (b) the scale bars correspond to 300 nm. (c) Current ratio between P_{up} and P_{down} states as a function of the PZT thickness.

In addition, the overall tunneling behavior depends on the thickness of the ferroelectric layer.[49] At the thin limit, direct quantum tunneling can be expected, while Fowler-Nordheim tunneling governs the out-of-plane transport for samples with thicker PZT layers. More detailed discussions on the tunneling behavior can be found in Supporting Information. The current ratio in our heterostructure (x = 0.20) between the upward and downward FE polarizations was obtained as a function of the PZT thickness, as shown in Figure 22c. It exhibited a peak around 7 nm of PZT. This behavior implies that there is an optimal thickness of the FE layer for the largest TER effect. When the thickness of the FE layer was too thin, the tunneling current was very large even for downward polarization, so the contrast seemed to be diminished. Also, as the PZT thickness approaches the critical thickness of ferroelectricity, the polarization decreases due to the enlarged effect of the depolarization field.[98,100] Since an increased polarization should result in a larger TER effect,[52] the decreased TER effect for thinner PZT might also be attributed to weakened ferroelectricity and increased leakage currents. On the other hand, when the PZT thickness is larger than ~10 nm, tunneling through the PZT layer would become extremely difficult, which again decreases the TER ratio. This reduction is caused by the exponential decrease of the tunneling probability as the thickness of the barrier layer increases. Note that the TER ratio for our PZT/LSMO heterostructure with the optimal PZT thickness (7 nm) is at least 30,000%. The actual

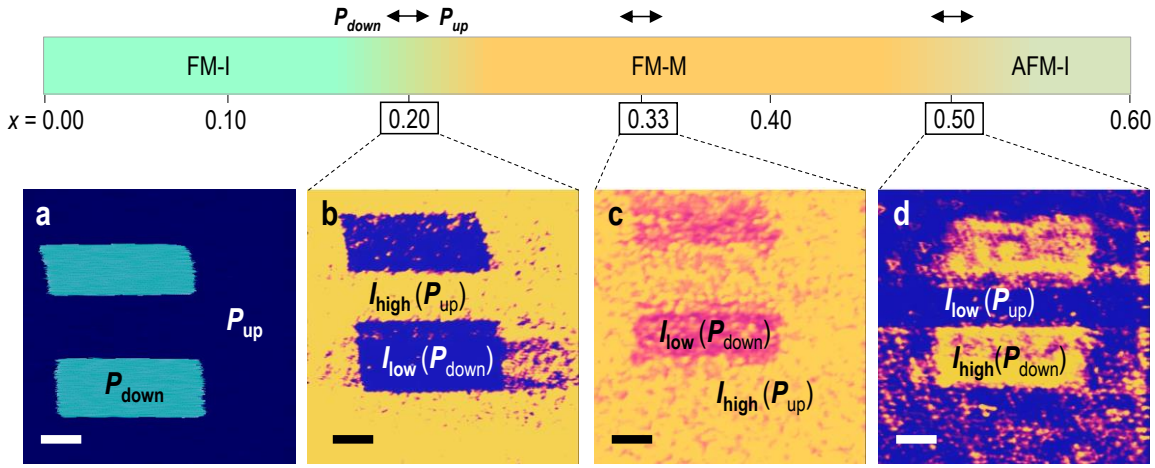

Figure 23. Tunneling current modulation at various phase boundaries.

(a) PFM phase and (b to d) CAFM images of the PZT/LSMO heterostructure for compositions (b) x = 0.20, (c) 0.33, and (d) 0.50 at room temperature. The FE polarization induced phase transition in LSMO is shown via arrows. The scale bars on the images correspond to 300 nm. See Figure 22 for data scale bars.

value could be larger, but due to instrumental limitations, we calculated the ratio with the measurable minimum current level of 10 pA. The TER ratio is significantly larger than those reported in other heterostructures,[84,85,91,93,101] or comparable with some previous reports.[83,86,102] Note that in those studies, the TER effect was solely attributed to the FE layer. Therefore, the large TER effect in our optimized PZT/LSMO heterostructure unveils the important role of the CEO layer. As observed from the in-plane transport in Figure 21a, the modified phase of LSMO due to the FE polarization largely amplifies the electroresistance effect. Note that using non-FE oxides such as $LaAlO_3$ for the PZT layer or $SrRuO_3$ for the LSMO layer have revealed no such huge electroresistance effect, suggesting that the phase modulation in the CEO layer is mostly responsible for the observed TER effect.

More importantly, we believe that the LSMO CEO layer could play a more crucial role than the PZT FE layer for the electroresistance effect in the heterostructures. To examine this idea, we varied x in our LSMO layer deposited prior to the PZT layer (10 nm in thickness). Figure 23 shows CAFM images for x = 0.20, 0.33, and 0.50 in LSMO, taken at room temperature. A typical PFM phase image representative for all PZT/LSMO heterostructures confirmed the good ferroelectricity of PZT as shown in Figure 23a. It consistently displayed both positively and negatively poled domains with a clear contrast, regardless of x. On the other hand, the resultant TER effect observed from the CAFM image was strikingly different. For the x = 0.20 heterostructure, as already shown in Figure 21, the upward (downward) polarization resulted in a significantly high (low) tunneling current. Surprisingly, for the x = 0.50 heterostructure,

this TER trend was completely reversed. As shown in Figure 23d, for x = 0.50, the upward (downward) polarization resulted in a low (high) tunneling current, with a similarly distinct contrast in the current level as in the x = 0.20 heterostructure. On the other hand, the x = 0.33 heterostructure showed similar trends as the x = 0.20 heterostructure, but the contrast between the current level for the upward and downward polarizations was substantially suppressed.

In these regards, it is worthwhile mentioning again that the FE polarization in the PZT layer induces a hole-accumulated or -depleted state in LSMO near the interface. These changes in the hole carrier density near the interface could drastically alter the electronic and magnetic states of LSMO, especially when x is near a phase boundary.[96] The distinctly different phase of LSMO would of course change the boundary condition at PZT/LSMO interface dramatically, influencing the tunneling current that we observe in the CAFM measurement. Note also that the x = 0.20 and 0.50 LSMO heterostructures are in the vicinity of different phase boundaries. In fact, x = 0.20 and 0.50 transit, respectively, from insulating and metallic phases to metallic and insulating phases by hole accumulation. Since the metallic (insulating) phase of LSMO would increase (decrease) the tunneling probability across the heterostructure, the opposite trend in the CAFM can be easily understood by taking into account the polarization-induced modulation of electronic states in LSMO. Furthermore, the x = 0.33 LSMO is in the middle of the metallic phase which manifests that the FE field effect on the LSMO layer is weakened. Note that this suppressed contrast is in agreement with what most previous reports have observed with x ~ 0.30 LSMO or SRO.[84,85]

Some of the effects described here have been further verified by theoretical calculations. A microscopic model Hamiltonian was employed to simulate the depletion/accumulation of holes on the CEO side of the structure. More specifically, the Hamiltonian contains the standard two-orbital double-exchange (DE) term supplemented by an electrostatic potential originating from the surface charge of PZT that is expected to induce a redistribution of e_g electrons in LSMO.[103] The FE polarization of PZT was modeled via a surface charge (±0.8 electrons/unit cell) attached to the LSMO interface, a reasonable and widely-accepted procedure.[103] Afterwards, the e_g profile and screening potential in LSMO were calculated self-consistently by diagonalizing the DE Hamiltonian and solving the Poisson equation for the electrostatic field.[103] The localized spins in the DE model were assumed to be FM for x = 0.20 and 0.33, and A-type AFM (A-AFM) for x = 0.50, or paramagnetic (PM), *i.e.* disordered for all the values of x studied here. Note that the results for the change in carrier populations were found to be quite similar leading us to conclude that the observed hole redistribution is dominated by electrostatics. As shown in Figure 24 and discussed previously, the screening effect on the LSMO layer is mostly restricted to just a few layers from the interface.[96] Although the screening length depends on the LSMO effective dielectric constant used, the qualitative tendencies are unambiguous: when the FE polarization points away from the LMSO layer, the interfacial e_g density is

prominently decreased (*i.e.* holes are accumulated). In contrast, the interfacial hole density is suppressed when the FE polarization points towards the LSMO layer. The FE modulation of the e_g density near the interface is expected to modify the interfacial physical properties of LSMO significantly, in accord with well-established Mn-oxide theoretical phase diagrams and also with a recent prediction.[104] This interfacial phase transition will induce drastic changes in both the in-plane conductance and the out-of-plane tunnel current [87]. In fact, considering the x = 0.50 heterostructure as an example and using proper superexchange coupling, our calculation shows that the interfacial

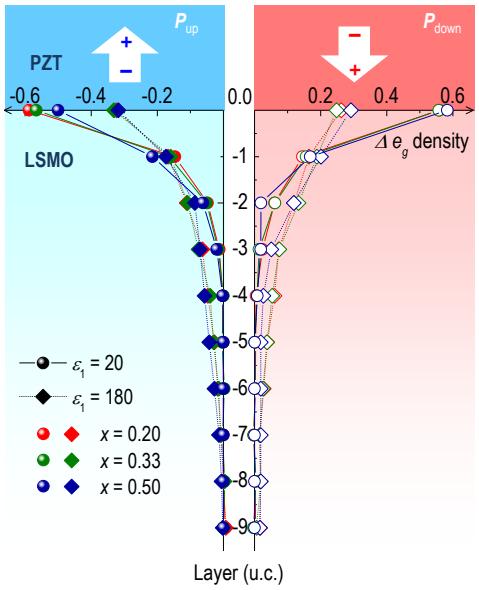

Figure 24. FE field control of interfacial charges.

The theoretical depth profile showing the changes in the e_g electronic density for upward (Q = –0.8) and downward (Q = 0.8) polarizations for compositions x = 0.20, 0.33 and 0.50. The spin configurations in the DE model were selected as FM for x = 0.20 and 0.33, and A-AFM for x = 0.50. Two different dielectric constants (ε_1 = 20 and 180) have been used to compare the degree of FE control. These idealized calculations show that the electronic density modifications in the first and second layers can indeed be very large, compatible with the experimental results. Our theoretical results define an upper bound of what could be achieved experimentally, since effects such as lattice reconstructions at the interfaces have not been incorporated. In the Supplementary Information, results for PM spin configurations are presented as well, showing that the amount of hole doping does not change much with the spin configuration.

LSMO layers may become FM instead of the original A-AFM ground state order.[79] The possible interfacial FM to A-AFM phase transition in the x = 0.20 heterostructure will give rise to the opposite effect. Note that our calculations were performed for the ground state, namely at zero-temperature. Nevertheless, the results are overall in good agreement with the experimental observations. Moreover, since the amount of hole doping is similar for FM, A-AFM, and PM spin configurations, the latter to be expected in the high temperature state of LSMO, our results are useful to understand the large TER ratio of the FE/CEO junctions (see Supplementary Information for the PM result). The substantial modifications in the e_g electronic density observed in our simplified model system indicate that the local phase transitions in LSMO near the interface can indeed be potentially dramatic, and this effect could be utilized for amplified electroresistance or other electronic devices that require large ON/OFF ratios.

Our combined experimental and theoretical observations robustly indicate that the modulated phase in LSMO is the key factor to control the TER, but the following additional details should also be considered for a deeper understanding of the system. First, the thickness of the LSMO should be carefully controlled, in addition to the PZT thickness, as it significantly influences the current ratios. As the LSMO thickness approaches the ultrathin limit, LSMO tends to exhibit the behavior of a film with a smaller doping.[105,106] Since our LSMO ultrathin films are only 5 nm thick, they could behave as less-than-nominally doped films. (Note that the thickness dependence could vary with the doping level x in LSMO) Although it would be rather difficult to quantify this thickness influence, the effect would simply shift the LSMO layer to a lower doping value in the vicinity of the phase boundaries of x = 0.20 and 0.50 LSMO. Thus, this is not a serious problem. Second, the depletion width for the carrier depleted state for the downward PZT polarization should be considered as well. This would be especially important for future quantitative analyses, as the depletion width could change for different electronic phases of LSMO. Since the depletion width would directly affect the tunneling probability across the heterostructure, it is an important parameter to be considered. Third, due to the phase changes in the LSMO layer, the PZT layer can be inversely affected. For example, drastic modifications in the boundary condition could alter the depolarization field, which could directly affect the FE polarization. Finally, intrinsic phase separation tendencies in the manganite layers could also be an issue to consider in real materials.

Conclusions

In conclusion, we have demonstrated that TER in ultrathin FE/CEO (PZT/LSMO) heterostructures is determined by phase transitions in the interfacial state of LSMO induced by the FE polarization. This coupled phase modulation was confirmed using LSMO layers with compositions near the phase boundaries. The largest TER ratio was obtained for LSMO x = 0.20, reaching a ratio > 30,000%. This implies that the polarization induced phase transitions in the LSMO layer play the most important role in

determining the value of the TER. Our effort not only provides a comprehensive understanding of the electroresistance behavior in strongly coupled systems, but also contributes to the exploration of nanoscale highly sensitive non-volatile electronics, in which two different tunneling resistances define the logic states by the influence of the FE polarization.

CHAPTER IV

FERROELECTRICS/CUPRATES HETEROSTRUCTURES

Since the resistance switch and tunneling electroresistance effect have been successfully demonstrated in PZT/manganites heterostructures and insulator-to-metal transition in LSMO is induced by field effect, we describe the results of the measurements on the PZT/cuprates heterostructures in this chapter, in order to study the insulator-to-superconductor transition in cuprates. Because the high-temperature superconductors have complicated structures and electronic properties, a group of external factors have huge influence on SC. So we discuss the strain and oxygen effect on cuprates first and then move on to the field effect on SC.

Epitaxial strain and oxygen stoichiometry effect on superconductivity of cuprates

Introduction

Since the discovery of high-temperature superconductivity (HTS) in the cuprate oxides in the 1980's[109], it has been generally believed that the superconductivity occurs within the copper oxide plane, CuO_2. Although the deep underlying mechanism of HTS has been a continuing controversial topic, it is well-known that the crystal lattice has a strong influence on superconductivity.[110-112] Since lattice change can be introduced by external stress, it has been found that the superconducting transition temperature (T_c) is affected under high stress, in which it decreases when the stress across CuO_2 plane while increases along the plane.[113-115] Therefore, due to the complete opposite effects of stress along *a* and *c* directions, in which $\partial T_c/\partial \sigma_a > 0$ and $\partial T_c/\partial \sigma_c < 0$, epitaxial strain becomes a more reliable parameter to study the lattice effects upon superconductivity. Thus $La_{2-x}Sr_xCuO_4$, evolving from an insulator to a superconductor when carriers are doped into the CuO_2 plane, is a very good candidate for strain effect studies, because its superconductivity is rather sensitive to the ratio of *a* and *c.*[116] A consensus has been achieved in numerous investigations that compressive strain increases T_c, even beyond the bulk value (T_c = 40 K), while the tensile strain suppresses it.[117-120,122] The main reasons are ascribed to the elongation along the *c* direction which results in change in electrostatic potential on Cu, suppression of the low-temperature tetragonal phase[121] and change in the charge stripes[122]. Besides strain, large enhancement or even initiation of superconductivity is also found by inserting additional oxygen in the LSCO lattice.[123-126] According to the three-band Hubbard model for LSCO[127], holes reside on the oxygen band; therefore excess oxygen redistributes carriers over the Cu-O

network.[128, 129] This has created a large interest in introducing post-growth oxidation in synthesis of LSCO films, because it is considered that the simplex parameter, such as strain, is not enough to fully increase the superconductivity. It was found that oxygen annealing can promote superconducting properties in undoped or lightly doped LSCO films.[125, 130] Up till now, a systematic determination of strain in conjunction with oxygen influences on LSCO has not been fully studied. In this chapter, we describe the results of the study both on the effects of strain and oxygen content on the optimally doped LSCO(x=0.15) and find that these two parameters are strongly coupled. Moreover, deeper understanding of energy preference of oxygen vacancies and lattice changes due to reduction and oxidation has been investigated in theoretical calculations.

Results and Conclusions

In order to systematically investigate the influence of strain and oxygen stoichiometry on LSCO, we have deposited optimally doped $La_{1.85}Sr_{0.15}CuO_4$films on (001)-orientated $LaSrAlO_4$ (LSAO), $LaAlO_3$ (LAO), $(LaAlO_3)_{0.3}(Sr_2AlTaO_6)_{0.7}$ (LSAT), and $SrTiO_3$ (STO) substrates by pulsed laser deposition (PLD). We have also varied the thickness of these films to determine the onset of superconductivity for the respective strained states. The details of the growth conditions are described later. The optimally doped LSCO(x = 0.15) has a tetragonal structure with the in-plane lattice constant a = 3.777 Å. Hence, LSCO films are under biaxial tensile stain on STO (a = 3.905 Å), LSAT (a = 3.868 Å) and LAO (a = 3.79 Å) with lattice mismatch of 3.27%, 2.35%, 0.34% respectively, and under compressive strain on LSAO (a = 3.755 Å) with -0.56% mismatch. The θ−2θ X-ray diffraction pattern reveals (00l) peaks, which clearly shows that our LSCO films are epitaxially grown in the c-orientated direction. Moreover, reciprocal space mappings (RSM) of X-ray patterns confirm that 0.34% mismatch from LAO and −0.56% from LSAO are fully strained states in LSCO samples, even when the film is thick enough. But even less than 1% variation in a_{LSCO} is sufficient to lead to drastic changes in the LSCO films. While the huge mismatch from LSAT and STO cannot easily persist in the LSCO films, in which tensile strain is substantially reduced due to lattice relaxation, to the value even smaller than that grown on LAO.

Because the electronic structure is one of the most determinant criteria of superconductors, the transport properties of these strained LSCO films are studied. The in-plane sheet resistances of these films were determined using a physical properties measurement system (PPMS, Quantum Design Inc.). Figure 25a is a summary of the T_c of LSCO films with varying thickness on each of the substrates. Among all the samples, the electronic state of LSCO starts from insulating due to the carrier depletion effect in ultrathin samples which is quickly suppressed in thicker films. The LSCO evolves from an insulator to a superconductor as the thickness increases closer to the bulk value. It is clearly shown in figure 1a that the onset T_c of all superconducting films are approximately 7 K, but when the epitaxial strain evolves from compressive to tensile, the thickness is dependent on T_c at a faster rate. Moreover, the onset thicknesses of LSCO under different strain states vary from one another. When 0.56% compressive

strain is applied from LSAO substrates, the onset thickness is 10 nm, while it exceeds 100 nm with 0.34% tensile strain on LAO. When the tensile strain is relaxed on LSAT and STO substrates, the onset thickness is reduced to 50 nm and 30 nm. Therefore, when the tensile strained films are significantly relaxed, the onset thickness also decreases drastically. The results match the traditional view that tensile strain kills the superconductivity while compressive strain promotes it. In thin film studies, it is considered that the profound influence from epitaxial strain is resulted from

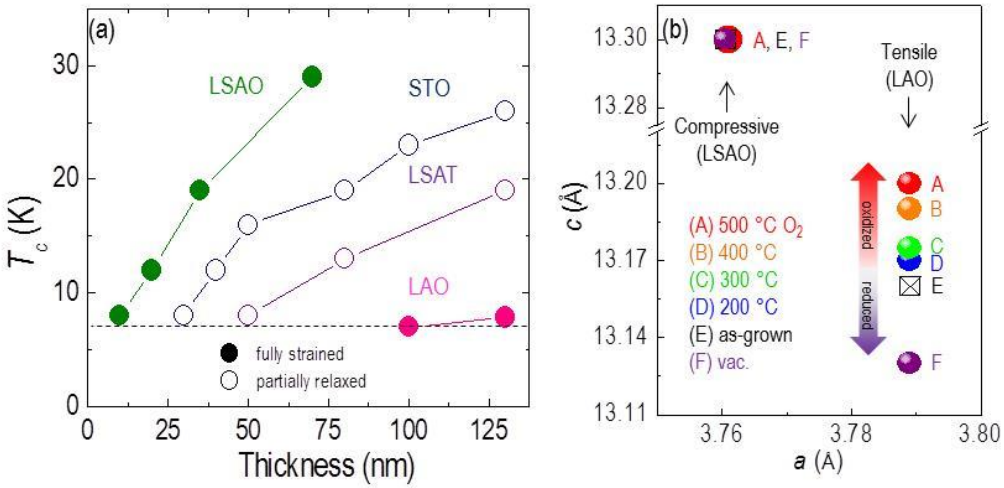

Figure 24. Strain dependent Tc and oxygen stoichiometry induced lattice change.

(a)Thickness dependence Tc of LSCO(x=0.15) films grown on LSAO, LAO, LSAT and STO substrates (b) Out-of-plane lattice constants of 20 nm thick LSCO(x=0.15) as-grown, annealed in oxygen and vacuum films on LAO substrates.

the change in the apical Cu-O bond length[116, 131, 132]. However, in some x-ray absorption studies, it is found that the in-plane Cu-O bond is the determinant factor for the superconductivity.[133, 134] Based on those controversial explanations, it is indicated that the mechanism of strain effect on superconductors are not easily determined from the lattice modulation, so more parameters should be involved.

In addition to strain, oxygen stoichiometry has also been reported as a crucial factor for superconductivity in cuprate oxides. As reported in earlier studies, post-annealing in highly oxidizing atmospheres such as ozone-oxygen mixtures is introduced to sufficiently increase T_c in LSCO. And it is discovered that such post-growth treatment can insert extra oxygen atoms into interstitial positions, which has larger influence on underdoped cuprates than optimally doped ones.[125] Since it is well known that oxygenation effect in oxides is usually accompanied with lattice alteration which also

creates strain effect, we assume that oxygenation and strain can interact with each other. So we introduce a strain-dependent oxygen content study on LSCO by performing post annealing process on LSCO films to explore comprehensive understanding of the dependence of these two factors. The lattice change of the tensile (LAO) and compressive (LSAO) strained LSCO during post annealing is shown in Figure 25b. Here, the in-plane constants are fixed by stress, and the *c* lattice parameter is possible to be altered by oxygen sponge. And we found that in compressive strained case (LSCO/LSAO), little variation resulted from oxidization process. On the contrary, under tensile strain films have large lattice parameter changes along the *c* direction,

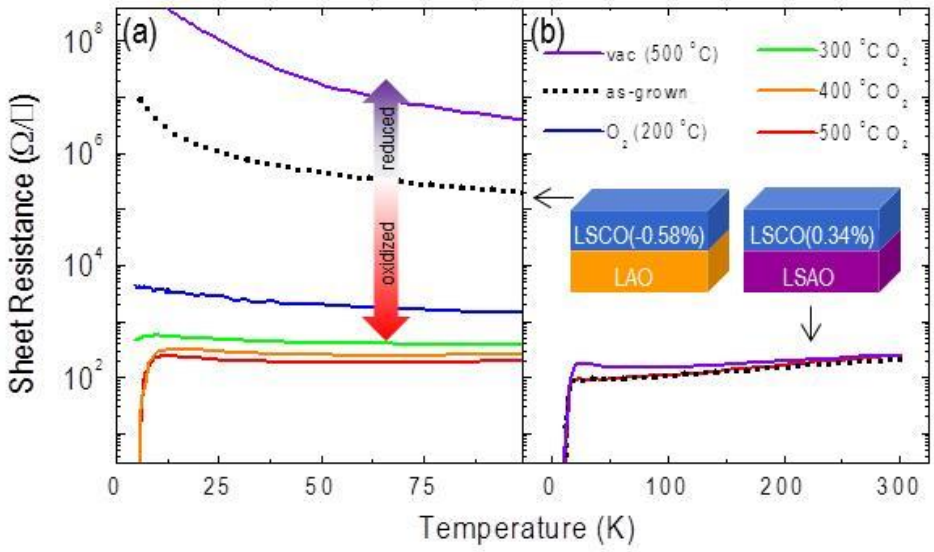

Figure 25. Strain and oxygen content control of superconductivity.

Temperature dependent sheet resistances of LSCO(x=0.15) as-grown, annealed in oxygen and vacuum films (a) on LAO substrates (b) on LSAO substrates

in which large expansion during oxidization and contraction during oxygen reducuction process are seen. Furthermore, the oxygen annealing temperature is extremely important for lattice expansion. For the same annealing time, the greater the temperature, the more increase is introduced to the *c* lattice constant in LSCO films. Longer oxidation time fails to bring more change into the system. Therefore, tensile strain makes the cuprate lattice rather sensitive to oxygen sponge while compressive strain stabilizes the oxygen sublattice of the cuprate very well. Especially, the trend of lattice change is contrary to that in perovskite oxides in which contraction is found in oxidization process due to attraction of electron cloud by extra oxygen. But our unreasonable lattice changes still have some clues in earlier studies. Even though it has been briefly explained that expansion during oxygenation is ascribed to interstitial oxygen insertion and contraction in oxygen reduce is resulted from removal of apical

oxygen[15], we need deeper exploration to determine whether it is really the case in our LSCO(x=0.15) systems.

In-plane transport measurements of these annealed and as-grown LSCO films have also been carried out. The data are shown in Figure 26. Altering the oxygen content via post-annealing affects not only the structural properties but the sheet resistance as well. The as-grown LSCO is 20 nm, which is thin enough to sustain the full strain from the substrates, during vacuum annealing at 500 °C and 10^{-4} Torr, the resistivity is increased by more than one order of magnitude. During oxygen annealing at 200 °C 400 Torr O_2, the resistivity is reduced by more than two orders of magnifude. As the oxidization temperature increases up to 400°C, the resistivity decreases and eventually the film becomes superconducting near 12 K. Bearing this in mind, the oxidization temperature is the most critical factor to lower the oxygen migration barrier in tensile-strained films.

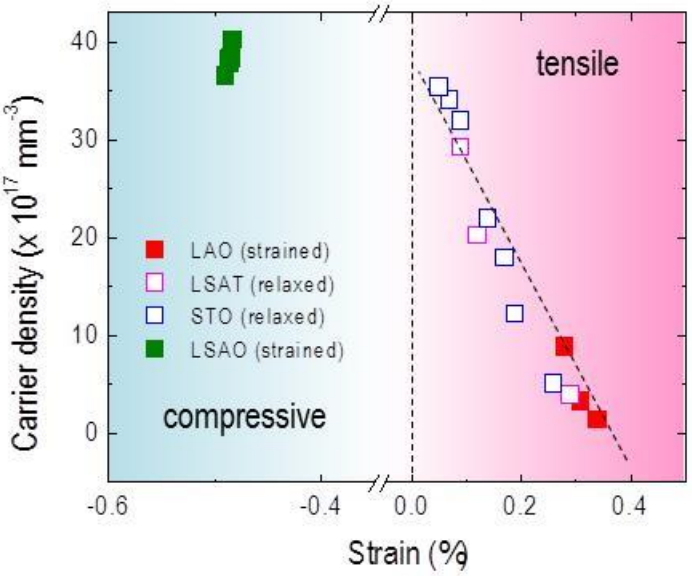

Figure 26. Carrier density modulation mediated by strain states.

Carrier densities of LSCO(x=0.15) under tensile and compressive strain. The dashed line corresponds to the linear relationship of strain state and carrier density.

While for LSCO under compressive strain, superconductivity is retained, regardless of vacuum or oxygen post-annealing. These results are consistent with the lattice change trend during annealing, revealing an ‘oxygen sponge’ behavior of LSCO where tensile strain can move oxygen in and out of the lattice easily while compressive strain may retain it under all post-annealing environments.

It is very evident from these studies that epitaxial strain is strongly coupled with the oxygen stoichiometry. In our studies, especially those shown in Figure 26, oxygen can easily move in and out of the cuprate lattice in tensile strained films and difficult to tune electronic properties of compressive strained cuprate films. This indicates that the acknowledged discovery that tensile strain kills the superconductivity is not only due to lattice modulation (the change in Cu-O bond length) as reported, but also because that it triggers the change in oxygen stoichiometry of LSCO. Therefore tensile strain will facilitate oxygen vacancy formation in LSCO films, which is an important reason why superconductivity is easily suppressed under vacuum annealing. While the LSCO films are fully oxidized under compressive strain which can sustain the oxygen content. Moreover, in tensile-strained cuprates, the oxygen diffusion barrier is lowered, and then oxygen migration through the lattice becomes much easier. So epitaxial strain can tune the oxygen content in LSCO and modify the oxygen migration across the lattice as well.

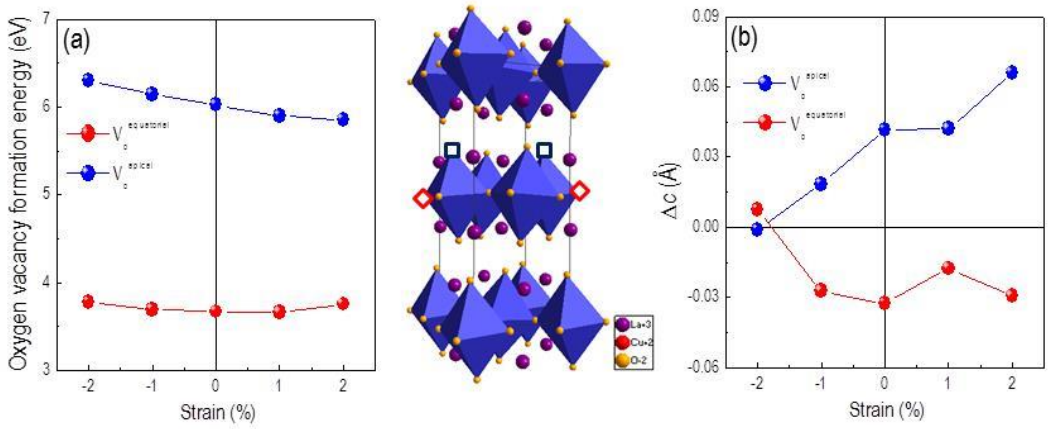

Figure 27. Preferential site for oxygen vacancy formation and lattice response of oxygen vacancy formation.

(a) Strain dependent formation energies of equatorial and apical oxygen vacancies (b) Strain and oxygen vacancy site dependent c lattice constants change.

Since a subtle change in oxygen stoichiometry can result in notable difference in the holes doped into LSCO, we carried out carrier density measurements on LSCO to further confirm the strong coupling between epitaxial strain and oxygen content. As shown in Figure 27, the carrier densities of LSCO films grown on different substrates with varying thicknesses have been summarized. The epitaxial strain is calculated from the mismatch between the in-plane lattice constants of the film and bulk value. When

LSCO films are fully strained, as grown on LAO and LSAO, the strain is maintained for large thicknesses. When the film is partially strained (grown on LSAT and STO), the extent of the relaxation has a large fluctuation as the film grows thicker. The carrier densities of tensile strained LSCO change significantly as a function of the degree of strain. When tensile strain is relaxed about 0.3%, the carrier density is increased roughly 30 times from the fully strained state, which indicates that the carrier density and the strain have almost a linear relationship. This illustrates that the carrier density in cuprate films is strongly correlated with the epitaxial strain, which is due to the change in oxygen content.

even though we believed that under tensile strain oxygen vacancies are formed and oxygen migration is eased, deeper insights of the oxygen sublattice in LSCO should be developed. For one thing, according to the symmetry of LSCO, there are two possible positions for oxygen vacancies to reside: equatorial (in CuO_2 plane) and apical (perpendicular to CuO_2 plane) positions. So the question of where the oxygen vacancies triggered by tensile strain is located has been raised. For another, the abnormal lattice change during oxidization and oxygen reduction processes needs explanation. Although the expansion along the out-of-lane direction in oxygenation has been understood by inserting oxygen into interstitial positions so far, it cannot completely be convinced due to our observations. Since we suppose that intrinsic oxygen vacancies are induced in tensile strained LSCO films, the oxygen is more likely to fill the vacancy positions rather than staying in interstitial positions. Furthermore, the Hall measurements of as-grown and annealed films show that carrier density is changed with oxygen moving in and out. But the interstitial oxygen is known to be highly mobile, but it is difficult to contribute to the modulation of the carrier concentration. In order to find reasonable answers to this puzzle, Density Function Theory (DFT) is carried out, as shown in figure 28.

Through these theoretical calculations, it was found that the oxygen vacancy is always more stable under tensile strain for both apical and equatorial positions. The formation energy of apical oxygen vacancy is around 6 eV which is much higher than the formation energy of equatorial oxygen vacancy which is around 3 eV. From these results, we conclude that there is a preferential formation of oxygen vacancies within the CuO_2 plane in the equatorial position as opposed to the apical position. This discovery is also a good illumination that tensile strain is a hindering factor of superconductivity. Moreover, we found a similar trend of lattice change in DFT calculations as in our experimental measurements. Regardless of the type of strain, tensile or compressive, when oxygen vacancy is located in the equatorial position, the *c* lattice constant becomes smaller than the bulk value while it is larger than the bulk value when oxygen vacancy is in the apical position. This result verifies that the tensile strain triggers equatorial oxygen vacancy formation.

Conclusions

In conclusion, our experimental studies consistently show that epitaxial strain is strongly correlated to the oxygen stoichiometry in LSCO as shown by the dramatic effects upon the superconductivity. Tensile strain facilitates oxygen vacancy formation within the equatorial positions which has not been previously determined. Moreover, tensile strained LSCO films exhibit a remarkable oxygen sponge behavior while compressive strain does not. Though the underlying reason of lattice expansion and contraction according to oxidation and oxygen reduction is not well understood, these results bring more comprehensive understanding on superconductivity.

Superconductivity induced by field effect in overdoped cuprates

Introduction

The superconducting cuprate oxides have a complicated phase diagram and are quite sensitive to external stimulus due to the strong electron correlation. The ground state of cuprates can be manipulated through a slight variation of carrier concentration, which results in drastic change in physical properties. Besides chemical doping, electrostatic effect, especially through ferroelectric control, is also a useful tuning method, because it is a controllable and reversible. The ferroelectricity induced carrier population change, which leads to drastic phase transitions, has been studied in many functional oxides materials. In previous studies, it has been demonstrated that ferroelectric control can effectively induce superconductivity and tune the critical temperature T_c.

In the $La_{2-x}Sr_xCuO_4$ (LSCO) system, the superconductivity is influenced by many factors, such as the low temperature tetragonal phase, charge stripes, strain states and so on. It has been reported that superconductivity can be created in undoped and lightly doped region by compressive epitaxial strain or by ozone annealing, in which abnormal high T_c appears when Cu-O bond length is modulated or extra oxygen is inserted into the lattice. But these methods unavoidably introduce defects and disorder in the crystal when superconductivity is turned on. Moreover, interface superconductivity has been observed in undoped and overdoped cuprates heterostructures, although the underlying reason has not been uncovered yet. But deeper exploration on this heterostructure has found that this superconductivity resides in the undoped layer. Therefore, nearly all of the induced superconductivity evolves from the undoped antiferromagnetic insulator phase. Thus it is likely that the strong spin correlation in the antiferromagnetic phase is required for the formation of Cooper pairs. Up till now, field effect induced superconductivity has not been observed and the possibility of superconductivity in overdoped phase has not been tested. In this report, we demonstrate the ferroelectric introduced superconductivity in the overdoped cuprates LSCO (0.4). We also show that the superconductivity can be easily turned on and off by different polarization directions of PZT in PZT/LSCO heterostructures.

Results and Discussions

In order to test the field effect on the superconducting state and T_c, we deposited a group of LSCO (0.15) and $Pb_{0.8}Zr_{0.2}TiO_3$ (PZT) heterostructures by pulsed laser deposition on (001) $LaAlO_3$ (LAO) and $SrTiO_3$ (STO) substrates. The typical polarizations of PZT were around 80μC/cm^2, with little thickness fluctuation. The details on the growth can be found elsewhere. The spontaneous polarization and ferroelectricity of PZT is determined by piezoresponse force microscopy (PFM) as shown in Figure 29 The polarization was switched by a conductive AFM tip using the applied field of +5 and -5 V. The PFM phase images of PZT grown on LAO shows that it has a single domain with downward switchable polarization.

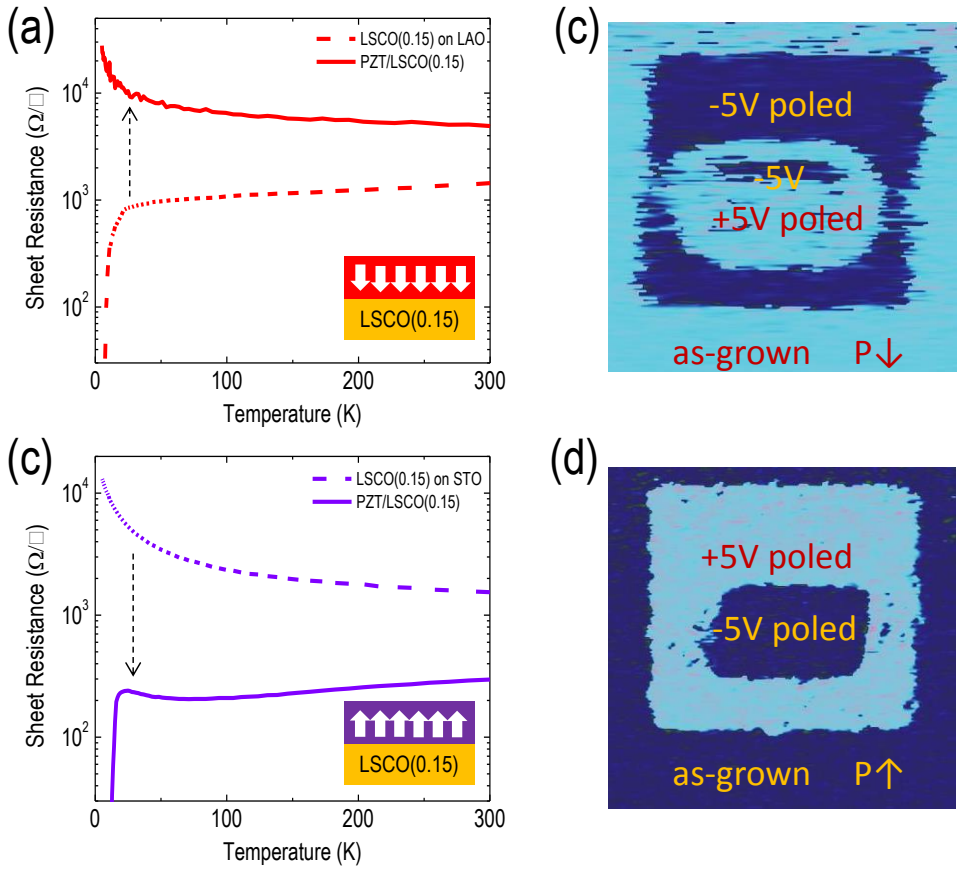

Figure 28. Ferroelectric switch of superconductivity

(a) T-dependent sheet resistance curves of LSCO (0.15) and PZT 10nm/LSCO (0.15) 100nm on LAO substrate (b) PFM image of PZT/LSCO (0.15) heterostructure on LAO and the dark blue region corresponds to -5V poled region while the light blue region corresponding to +5V pole region (c) T-dependent sheet resistance curves of LSCO (0.15) and PZT/LSCO (0.15) 15nm on STO substrate (d) PFM image of PZT/LSCO (0.15) heterostructure on STO

The temperature (*T*)-dependent sheet resistance curves, *R(T)*, of these samples were recorded by a physical property measurement system (PPMS, Quantum Design Inc.). The 100nm LSCO (0.15) on LAO is superconducting, with T_c around 8K. Thinner films are insulating due to tensile strain from the LAO substrates. Its *R(T)* curve is comparable with the samples capped by a 10nm PZT layer. The result reveals that we can successfully turn off the superconductivity not by tuning chemical doping but through the field effect from a ferroelectric capping layer. The downward polarization in PZT can introduce electron doping in the underneath layer LSCO (0.15), which leads to the superconductor-to-insulator transition.

On the contrary, when we grew the PZT/LSCO heterostructures on STO substrates, the as-grown PZT is also in single domain but with upward polarization as shown in the PFM phase image in figure…. The opposite direction of polarization is probably due to difference in the strain from the substrate or the termination, but the exact reason is not very clear yet. The LSCO on STO is 15nm thick, under tensile strain and in the oxygen-deficient state (as mentioned in the strain effect study of the cuprates). So this LSCO layer is off from the optimally doping phase but resides in the lightly-doped region; and when PZT is deposited above LSCO with upward polarization (PZT/LSCO heterostructures), LSCO returns back to a superconductor. Therefore, the upward polarization effectively induces the hole accumulation in the LSCO films and turn on the superconductivity.

Since the modulation of superconductivity in optimally doped cuprates can be realized by the polarization of PZT, we further tested this effect on overdoped cuprates. When cuprates is in the overdoped region, it is known as a Fermi liquid, in which high carrier concentration and weakened electron correlation have annihilated the superconductivity. So a group of LSCO (0.4) and PZT heterostructures on LAO substrates were synthesized. As mentioned above the PZT deposited on LAO has an downward polarization with single domain, and can trigger electron doping in the underneath layer. The LSCO (0.4) layer is fixed at 20nm and PZT layers are varied as 5, 10 and 30nm. The sheet resistance curves *R(T)* of these samples are shown in figure 30.

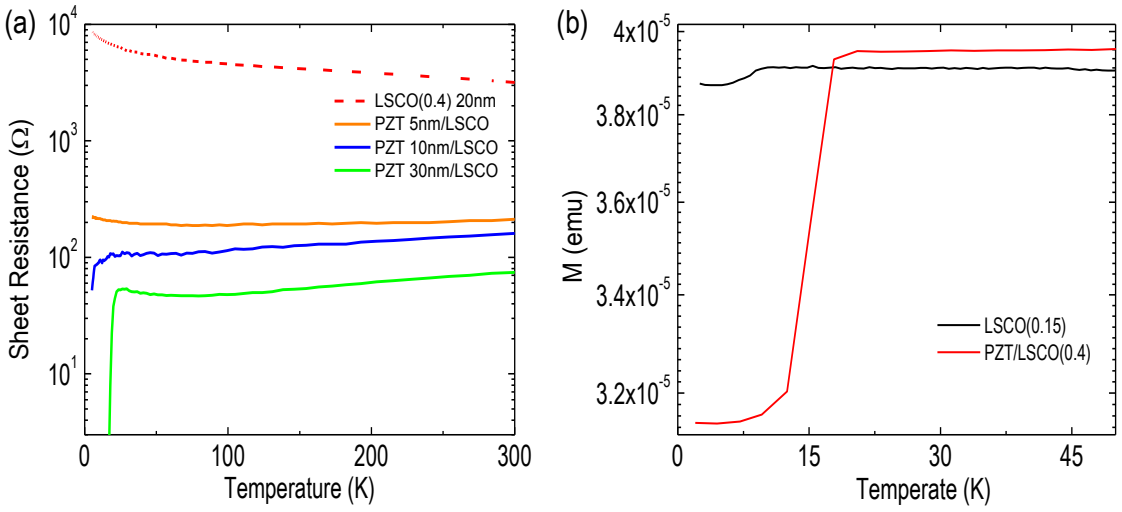

Figure 29. Interface superconductivity of PZT/LSCO

(a)T-dependent sheet resistance curves of LSCO (0.4) 20nm and PZT/LSCO (0.4) 20nm heterostructures, and the thicknesses of PZT vary as 5, 10 and 30nm. (b) T-dependent magnetization curves of 100nm LSCO(0.15) and PZT 30nm/LSCO (0.4).

It is clear that the ferroelectric capping layer brings drastic modulation to the conducting properties of the overdoped cuprates. Even under ultrathin PZT film (5nm), nearly 2 orders of magnitude change in sheet resistances can be realized in the LSCO (0.4) layer. Though the LSCO becomes more conducting, it still shows a semiconducting behavior. When PZT is increased to 10nm, the transport property of LSCO becomes metallic, in which the resistance is reduced as temperature decreases. A trend of resistivity to fall down is shown near 5K, which indicates the possibility to trigger superconductivity in the overdoped cuprates. And finally in PZT 30nm/LSCO (0.4) heterostructures, the insulator to superconductor transition is introduced at the interface by the field effect, with T_c around 15K. Therefore, as the thickness of PZT film increases, the polarization in the ferroelectric layer becomes stronger, and when the field effect is large enough, superconductivity can be turned on in the over-doped metallic phase region of cuprates.

Besides the electronic behavior, another important criteria of superconductor is diamagnetism. So the T dependent magnetic moment curves, *M(T)* at 100Oe and 2K, of the cuprates heterostructures were recorded using a 7 T superconducting quantum interference device (SQUID, Quantum Design Inc.) magnetometer. *M(T)* curves of the PZT 30nm/LSCO (0.4) and 100nm LSCO (0.15) are compared in figure (b). They show that the T_c of LSCO (0.15) is around 8K while the PZT/LSCO (0.4) has a T_c around 15K, so these results support the T_c revealed in *R(T)* curves. Furthermore, the interface superconductor has a stronger diamagnetism, because the magnetic moment drops

down quickly, whereas the *M* of LSCO (0.15) decreases much more slowly. The heterostructure has a larger susceptibility than the optimally cuprates film on STO.

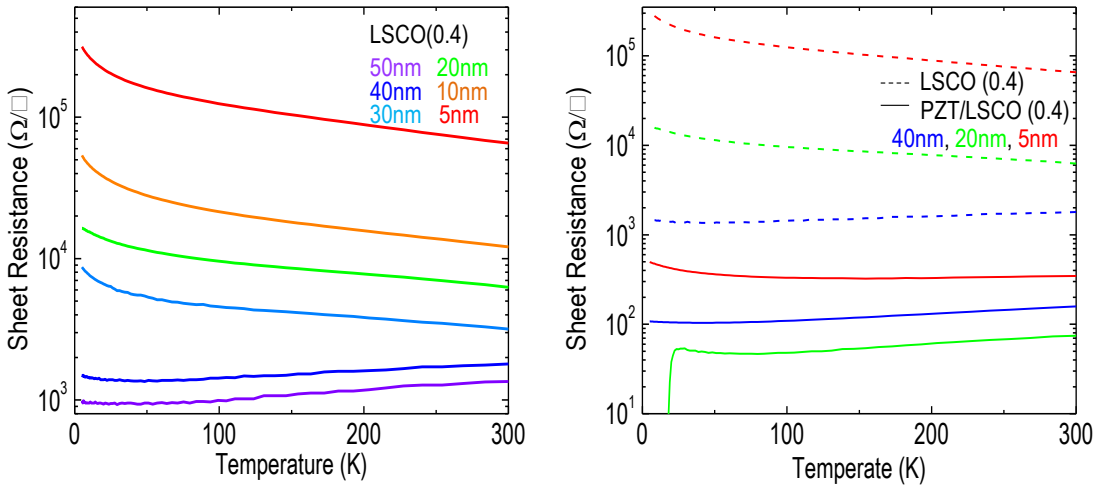

Figure 30. Thickness dependent properties of LSCO(0.4) and PZT/LSCO(0.4)

(a) T-dependent sheet resistance curves of LSCO (0.4) films and the thickness varies as 5, 10, 20, 30, 40 and 50nm. (b) T-dependent sheet resistance curves of LSCO (0.4) 5, 20, 40nm and PZT 30nm/LSCO (0.4) heterostructures

To further study the dependence of ferroelectric field effect on the thickness of LSCO (0.4), we grew a group of LSCO (0.4) films, whose thicknesses are varied as 5, 10, 20, 30, 40, 50nm. *R(T)* curves of these samples reveal that transport properties of LSCO(0,4) evolve from insulating to metallic as the thickness grows, as shown in figure 31 The critical thickness is around 30nm. When LSCO (0.4) film is thinner than 30nm, it behaves as an insulator due to carrier depletion; and when it is thicker than 30nm, it is metallic and the resistance decreases as the temperature drops. We then deposited PZT of 30nm on top of the 5, 20 and 40nm LSCO (0.4) films. The bare 5 and 20nm LSCO (0.4) are all insulating but the *R(T)* curves show that their resistances decrease by more than 2 orders of magnitude when they are covered by PZT. With the cover of PZT the 20nm LSCO (0.4) becomes superconducting while the sheet resistance of 5nm LSCO (0.4) shows a slight increase below 50K. Moreover, the bare 40nm LSCO (0.4) is metallic, and when it is under the field effect, the resistance is reduced by around one order of magnitude. So the field effect on LSCO is similar as what we discussed on LSMO in chapter 3; the carrier population change happens only in the few layers of the film underneath.

Conclusions

In summary, drastic changes in the electronic properties of LSCO films under the influence of ferroelectric polarization have been demonstrated. The effects from the PZT with opposite electrical polarization reveal that superconductivity of the optimally doped cuprates LSCO (0.15) can be turned on and off. Moreover, this field effect can introduce even the insulator-to-superconductor transition in the overdoped cuprates LSCO (0.4). This interface superconductor has strong diamagnetism and high susceptibility. The ferroelectric control is effective only in few layers of the cuprates film. Our observations demonstrate the possibility of superconductivity in overdoped region of cuprates, which brings broader application of field effect devices and more comprehensive understanding of interface superconductivity.

CHAPTER V
CONCLUSIONS

In conclusion, we performed neutron scattering on $NaNbO_3$ to probe the local and global structures of this ferroelectric material. The six phases with varying symmetries are determined from the average structures of this compound. Then the pair distribution function (PDF) studies have shown that the local structure is different from the long-range lattice structure and elucidated how it finally determines spontaneous polarization in ferroelectrics. The application of the field effect of ferroelectric oxides are investigated in ferroelectrics/manganties and ferroelectrics/cuprates heterostructures. Drastic change in resistivity by more than 4 orders of magnitude has been achieved in ultrathin PZT/LSMO heterostructures, which triggers insulator-to-metal transition and magnetization enhancement in LSMO. In addition, we find that the strongest coupling of ferroelectric resides in the thinnest bilayers. Then the switching on and off of superconductivity by spontaneous polarizations are demonstrated in the heterostructures of PZT and optimally doped cuprates. Most importantly, the interface superconductivity is introduced by field effect for the first time in overdoped cuprates which is originally in the Fermi liquid and metallic phase region.

The comprehensive understanding of the ferroelectricity in the compound $NaNbO_3$ brings us a deeper view at the atomic scale of the polarization formation, which has not been known for a long time, because attention has always been focused on the long-range structure. This discovery opens the possibility to find more lead-free ferroelectric compounds and enables better use of ferroelectric materials. The successful demonstration of the field effect induced phase transitions in PZT/LSMO and PZT/LSCO, as well as the colossal tunneling electroresistance effect in PZT/LSMO offer possibilities of promising device designs in the electronic industry, which can also benefit the industry of information technology.

REFERENCES

1 J. G. Bednorz and K. A. Müller, Z. Physik B - Condensed Matter **64**, 189 (1986).
2 M.K.Wu, J.R. Ashburn, C.J. Torng, P.H. Hor, R.L. Meng, L. Gao, Z.J. Huang, Y.Q. Wang, C.W. Chu, *Phys. Rev. Lett.* **58**, 908 (1987)
3 H. Maeda, Y. Tanaka, M. Fukutomi, T. Anaso, *Jpn. J. Appl. Phys. Lett.* **4**, L209 (1988)
4 A. Schilling, M. Cantoni, J.D. Guo, H.R. Ott, *Nature* **363**, 56 (1993)
5 R.J. Cava, R.B. van Dover, B. Batlogg, E.A. Rietmann, *Phys. Rev. Lett.* **58**, 408 (1987)
6 J. P. Locquet, J. Perret, J. Fompeyrine, E. Machler, J. W. Seo, and G. Van Tendeloo, Nature **394**, 453 (1998)
7 J. P. Locquet, J. Perret, J. Fompeyrine, E. Machler, J. W. Seo, and G. Van Tendeloo, Nature **394**, 453 (1998)
8 B. O. Wells, Y. S. Lee, M. A. Kastner, R. J. Christianson, R. J. Birgeneau, K. Yamada, Y. Endoh, and G. Shirane, Science **277**, 1067 (1997)
9 H. E. Mohottala, *Nature Materials* **5**, 377 - 382 (2006)
10 J. M. Tranquada, B. J. Sternlieb, J. D. Axe, Y. Nakamura, and S. Uchida, Nature **375**, 561 (1995)
11 J. Orenstein1 and A. J. Millis, *Science* **288**, 468 (2000)
12 G. Kotliar and J. Liu, *Phys. Rev. B* **38**, 5142 (1988).
13. Y. Suzumora *et al*., *J. Phys. Soc. Jpn.* **57**, 2768 (1988).
14 J. Valasek, *Phys. Rev*., **17**, 475 (1921).
15 V.L. Ginzburg, *Zh. Eksp. Teor. Fiz.,*, **15**, 739 (1946).
16 G.A. Smolensky and A.I. Agranovskaya, *Sov. Phys. Solid State*, **1**, 149 (1959).
17 T. Egami, Annual Review of Materials Research, Vol. 37: 297-315 (2007)
18 C. H. Ahn, J.-M. Triscone, and J. Mannhart, Nature, **424**, 1015 (2003)
19 D. Pantel *et al.,* ACS Nano, ***5,*** 6032 (2011)
20 D. Pantel et al., Nature Mater. DOI:10.1038 (2012)
21 A. Chanthbouala et al., Nature Nano. **7**, 101 (2011)
22 T Tybell, CH Ahn, JM Triscone , Appl. Phys. Lett. **75**, 856 (1999)
23 Tsymbal and Kohlstedt, Science **313**, 181 (2006)
24 R. E. Jaeger and L. Egerton, J. Am. Ceram. Soc. **45**, 209 (1962).
25 R. H. Dungan and R. D. Golding, J. Am. Ceram. Soc. **48**, 601 (1965).
26 G. H. Haertling, J. Am. Ceram. Soc. **50**, 329 (1967).
27 Y. Saito, H. Takao, T. Tani, T. Nonoyama, K. Takatori, T. Homma, T. Nagaya, and M. Nakamura, Nature **432**, 84 (2004).
28 C. N. W. Darlington and K. S. Knight, Physica B **266**, 368 (1999).
29 M. Ahtee, A. M. Glazer, and H. D. Megaw, Philos. Mag. **26**, 995 (1972).
30 I. Lefkowitzk, K. Lukazewicz, and H. D. Megaw, Acta. Crystllogr.**20**, 670 (1966).
31 O. Di´eguez, K. M. Rabe, and D.Vanderbilt,Phys. Rev. B **72**, 144101(2005).
32 Y. Shiratori, A. Magrez, and W. Fischer, J. Phys. Chem. C **111**,18493 (2007).
33 Helen D. Megaw, Ferroelectrics **7**, 87 (1974).
34 C. N. W. Darlington and H. D. Megaw, Physica B **29**, 2171(1973).
35 C. N. W. Darlington, Solid State Commun. **29**, 307 (1979).
36 K. Lukazewicz and H. D. Megaw, Acta Crystallogr. B **25**, 851(1969).
37 I. Tomeno, Y. Tsunoda, K. Oka, M. Matsuura, and M. Nishi, Phys.Rev. B **80**, 104101 (2009).

38 W. Zhong and D. Vanderbilt, Phys. Rev. Lett. **74**, 2587 (1995).
39 S. K. Mishra, R.Mittal, V. Y. Pomjakushin, and S. L. Chaplot, Phys.Rev. B **83**, 134105 (2011).
40 S.K. Mishra, N. Choudhury, S. L. Chaplot, P.S. R. Krishna, and R. Mittal, Phys. Rev. B **76**, 024110 (2007).
41 N.W. Thomas, Acta Crystallogr. Sect. B **52**, 1 (1996).
42 O. Hanske-Petitpierre, Y. Yacoby, J. M. De Leon, E. A. Stern, and J. J. Rehr, Phys. Rev. B **44**, 6700 (1991).
43 V. A. Shuvaeva, K. Yanagi, K. Yagi, and K. Sakaue, Solid State Commun. **106**, 335 (1998).
44 N. Bindzus and B. B. Iversen, Acta Crystallographica Section A **68**, 750 (2012).
45 T. Egami and S. J. L. Billinge, *Underneath the Bragg Peaks: Structural Analysis of Complex Material* (Pergamon, Oxford, 2003).
46 R. D. Shannon, Acta Crystallogr. Sect. A **32**, 751 (1976).
47 S. Hendricks and E. Teller, J. Chem. Phys. **10**, 147 (1942).
48 S. I. Raevskaya, I. P. Raevski, S. P. Kubrin, M. S. Panchelyuga, V. G. Smotrakov, V. V. Eremkin, and S. A. Prosandeev, J. Phys.:Condens. Matter **20**, 232202 (2008).
49 M. B. Salamon and M. Jaime, Rev. Mod. Phys. 73(3), 583 (2001).
50 Y. Tokura, Colossal Magnetoresistive Oxides (Gordon and Breach, London, 1999).
51 E. Dagotto, Phase Separation and Colossal Magnetoresistance (Springer, Berlin, 2002).
52 J. Z. Sun, D. W. Abraham, R. A. Rao, and C. B. Eom, Appl. Phys. Lett. 74(20), 3017 (1999).
53 J. Dho, N. H. Hur, I. S. Kim, and Y. K. Park, J. Appl. Phys. 94(12), 7670 (2003).
54 M. Huijben, L. W. Martin, Y. H. Chu, M. B. Holcomb, P. Yu, G. Rijnders, D. H. A. Blank, and R. Ramesh, Phys. Rev. B 78(9), 094413 (2008).
55 S. I. Khartsev, P. Johnsson, and A. M. Grishin, J. Appl. Phys. 87(5), 2394 (2000).
56 X. Hong, J. B. Yau, J. D. Hoffman, C. H. Ahn, Y. Bason, and L. Klein, Phys. Rev. B 74(17), 174406 (2006).
57 F. Tsui, M. C. Smoak, T. K. Nath, and C. B. Eom, Appl. Phys. Lett. 76(17), 2421 (2000).
58 S. Majumdar, H. Huhtinen, H. S. Majumdar, and P. Paturi, J. AlloysCompd. 512(1), 332 (2012).
59 E. Ertekin, V. Srinivasan, J. Ravichandran, P. B. Rossen, W. Siemons, A. Majumdar, R. Ramesh, and J. C. Grossman, Phys. Rev. B 85(19), 195460 (2012).
60 C. Adamo, X. Ke, H. Q. Wang, H. L. Xin, T. Heeg, M. E. Hawley, W. Zander, J. Schubert, P. Schiffer, D. A. Muller, L. Maritato, and D. G.Schlom, Appl. Phys. Lett. 95(11), 112504 (2009).
61 Y. Watanabe, Appl. Phys. Lett. 66(14), 1770 (1995).
62 T. Zhao, S. B. Ogale, S. R. Shinde, R. Ramesh, R. Droopad, J. Yu, K. Eisenbeiser, and J. Misewich, Appl. Phys. Lett. 84(5), 750 (2004).
63 M. Sirena, E. Kaul, M. B. Pedreros, C. A. Rodriguez, J. Guimpel, and L. B. Steren, J. Appl. Phys. 109(12), 123920 (2011).
64 C. H. Ahn, J. M. Triscone, and J. Mannhart, Nature 424(6952), 1015 (2003).
65 S. Dong, X. Zhang, R. Yu, J. M. Liu, and E. Dagotto, Phys. Rev. B 84(15), 155117 (2011).

66 C. A. F. Vaz, J. Hoffman, Y. Segal, M. S. J. Marshall, J. W. Reiner, Z. Zhang, R. D. Grober, F. J. Walker, and C. H. Ahn, J. Appl. Phys. 109(7), 07D905 (2011).
67 J. S. Cross, K. Kurihara, and H. Haneda, J. Appl. Phys. 98(9), 094107 (2005).
68 J. Nuffer, D. C. Lupascu, and J. Ro¨del, Ferroelectrics 240(1), 1293 (2000).
69 H. N. Lee, S. M. Nakhmanson, M. F. Chisholm, H. M. Christen, K. M. Rabe, and D. Vanderbilt, Phys. Rev. Lett. 98(21), 217602 (2007).
70 D. K. Petrov, L. Krusin-Elbaum, J. Z. Sun, C. Feild, and P. R. Duncombe, Appl. Phys. Lett. 75(7), 995 (1999).
71 A. Moreo, S. Yunoki, and E. Dagotto, Science 283(5410), 2034 (1999).
72 W. S. Choi, D. W. Jeong, S. S. A. Seo, Y. S. Lee, T. H. Kim, S. Y. Jang, H. N. Lee, and K. Myung-Whun, Phys. Rev. B 83(19), 195113 (2011).
73 U. C. Chung, D. Michau, C. Elissalde, S. Li, A. Klein, and M. Maglione, Thin Solid Films 520(6), 1997 (2012).
74 Esaki, L. *Phys. Rev.* **1958,** 109, (2), 603-604.
75 Julliere, M. *Phys. Lett. A* **1975,** 54, (3), 225-226.
76 Josephson, B. D. *Phys. Lett.* **1962,** 1, (7), 251-253.
77 Tsymbal, E. Y.; Kohlstedt, H. *Science* **2006,** 313, (5784), 181-183.
78 Zhuravlev, M. Y.; Sabirianov, R. F.; Jaswal, S. S.; Tsymbal, E. Y. *Phys. Rev. Lett.* **2005,** 94, (24), 246802.
79 Velev, J. P.; Duan, C.-G.; Belashchenko, K. D.; Jaswal, S. S.; Tsymbal, E. Y. *Phys. Rev. Lett.* **2007,** 98, (13), 137201.
80 Kohlstedt, H.; Pertsev, N. A.; Rodríguez Contreras, J.; Waser, R. *Phys. Rev. B* **2005,** 72, (12), 125341.
81 Bilc, D. I.; Novaes, F. D.; Íñiguez, J.; Ordejón, P.; Ghosez, P. *ACS Nano* **2012,** 6, (2), 1473-1478.
82 Hinsche, N. F.; Fechner, M.; Bose, P.; Ostanin, S.; Henk, J.; Mertig, I.; Zahn, P. *Phys. Rev. B* **2010,** 82, (21), 214110.
83 Garcia, V.; Fusil, S.; Bouzehouane, K.; Enouz-Vedrenne, S.; Mathur, N. D.; Barthelemy, A.; Bibes, M. *Nature* **2009,** 460, (7251), 81-84.
84 Gruverman, A.; Wu, D.; Lu, H.; Wang, Y.; Jang, H. W.; Folkman, C. M.; Zhuravlev, M. Y.; Felker, D.; Rzchowski, M.; Eom, C. B.; Tsymbal, E. Y. *Nano Lett.* **2009,** 9, (10), 3539-3543.
85 Maksymovych, P.; Jesse, S.; Yu, P.; Ramesh, R.; Baddorf, A. P.; Kalinin, S. V. *Science* **2009,** 324, (5933), 1421-1425.
86 Chanthbouala, A.; Garcia, V.; Cherifi, R. O.; Bouzehouane, K.; Fusil, S.; Moya, X.; Xavier, S.; Yamada, H.; Deranlot, C.; Mathur, N. D.; Bibes, M.; Barthélémy, A.; Grollier, J. *Nat Mater* **2012,** 11, (10), 860-864.
87 Burton, J. D.; Tsymbal, E. Y. *Phys. Rev. Lett.* **2011,** 106, (15), 157203.
88 Vaz, C. A. F.; Hoffman, J.; Segal, Y.; Reiner, J. W.; Grober, R. D.; Zhang, Z.; Ahn, C. H.; Walker, F. J. *Phys. Rev. Lett.* **2010,** 104, (12), 127202.
89 Yin, Y. W.; Burton, J. D.; Kim, Y. M.; Borisevich, A. Y.; Pennycook, S. J.; Yang, S. M.; Noh, T. W.; Gruverman, A.; Li, X. G.; Tsymbal, E. Y.; Li, Q. *Nat Mater* **2013,** advance online publication.
90 Ramesh, R.; Spaldin, N. A. *Nat Mater* **2007,** 6, (1), 21-29.
91 Dagotto, E.; Hotta, T.; Moreo, A. *Phys. Rep.* **2001,** 344, (1–3), 1-153.

92 Hambe, M.; Petraru, A.; Pertsev, N. A.; Munroe, P.; Nagarajan, V.; Kohlstedt, H. *Adv. Funct. Mater.* **2010,** 20, (15), 2436-2441.
93 Pantel, D.; Lu, H.; Goetze, S.; Werner, P.; Kim, D. J.; Gruverman, A.; Hesse, D.; Alexe, M. *Appl. Phys. Lett.* **2012,** 100, (23), 232902-4.
94 Lee, H. N.; Nakhmanson, S. M.; Chisholm, M. F.; Christen, H. M.; Rabe, K. M.; Vanderbilt, D. *Phys. Rev. Lett.* **2007,** 98, (21), 217602.
95 Stadler, H. L. *Phys. Rev. Lett.* **1965,** 14, (24), 979-981.
96 Jiang, L.; Choi, W. S.; Jeen, H.; Egami, T.; Lee, H. N. *Appl. Phys. Lett.* **2012,** 101, (4), 042902-4.
97 Pantel, D.; Alexe, M. *Phys. Rev. B* **2010,** 82, (13), 134105.
98 Sai, N.; Kolpak, A. M.; Rappe, A. M. *Phys. Rev. B* **2005,** 72, (2), 020101.
99 Junquera, J.; Ghosez, P. *Nature* **2003,** 422, (6931), 506-509.
100 Zhuravlev, M. Y.; Wang, Y.; Maekawa, S.; Tsymbal, E. Y. *Appl. Phys. Lett.* **2009,** 95, (5), 052902-3.
101 Garcia, V.; Bibes, M.; Bocher, L.; Valencia, S.; Kronast, F.; Crassous, A.; Moya, X.; Enouz-Vedrenne, S.; Gloter, A.; Imhoff, D.; Deranlot, C.; Mathur, N. D.; Fusil, S.; Bouzehouane, K.; Barthélémy, A. *Science* **2010,** 327, (5969), 1106-1110.
102 Pantel, D.; Goetze, S.; Hesse, D.; Alexe, M. *ACS Nano* **2011,** 5, (7), 6032-6038.
103 Dong, S.; Zhang, X.; Yu, R.; Liu, J. M.; Dagotto, E. *Phys. Rev. B* **2011,** 84, (15), 155117.
104 Burton, J. D.; Tsymbal, E. Y. *Phys. Rev. B* **2009,** 80, (17), 174406.
105 Kim, B.; Kwon, D.; Song, J. H.; Hikita, Y.; Kim, B. G.; Hwang, H. Y. *Solid State Commun.* **2010,** 150, (13–14), 598-601.
106 Huijben, M.; Martin, L. W.; Chu, Y. H.; Holcomb, M. B.; Yu, P.; Rijnders, G.; Blank, D. H. A.; Ramesh, R. *Phys. Rev. B* **2008,** 78, (9), 094413.
107 Choi, W. S.; Rouleau, C. M.; Seo, S. S. A.; Luo, Z.; Zhou, H.; Fister, T. T.; Eastman, J. A.; Fuoss, P. H.; Fong, D. D.; Tischler, J. Z.; Eres, G.; Chisholm, M. F.; Lee, H. N. *Advanced Materials* **2012,** 24, (48), 6423-6428.
108 Salafranca, J.; Alvarez, G.; Dagotto, E. *Phys. Rev. B* **2009,** 80, (15), 155133.
109 J. G. Bednorz and K. A. Müller, Z. Physik B - Condensed Matter **64**, 189 (1986).
110 H. Oyanagi, J Supercond Nov Magn **20**, 613 (2007).
111 H. Oyanagi, C. Zhang, A. Tsukada, and M. Naito, Journal of Physics: Conference Series **108**, 012038 (2008).
112 M. Lang, et al., Physical Review Letters **69**, 482 (1992).
113 S. L. Bud'ko, J. Guimpel, O. Nakamura, M. B. Maple, and I. K. Schuller, Physical Review B **46**, 1257 (1992).
114 F. Gugenberger, C. Meingast, G. Roth, K. Grube, V. Breit, T. Weber, H. Wühl, S. Uchida, and Y. Nakamura, Physical Review B **49**, 13137 (1994).
115 M. Nohara, T. Suzuki, Y. Maeno, T. Fujita, I. Tanaka, and H. Kojima, Physical Review B **52**, 570 (1995).
116 C. Park and R. L. Snyder, Journal of the American Ceramic Society **78**, 3171 (1995).
117 J. P. Locquet, J. Perret, J. Fompeyrine, E. Machler, J. W. Seo, and G. Van Tendeloo, Nature **394**, 453 (1998).
118 D. Pavuna, D. Ariosa, D. Cloetta, C. Cancellieri, and M. Abrecht, Pramana - J Phys **70**, 237 (2008).

119 H. Oyanagi, N. L. Saini, A. Tsukada, and M. Naito, Journal of Physics and Chemistry of Solids **67**, 2154 (2006).
120 H. Oyanagi, A. Tsukada, M. Naito, and N. L. Saini, Physical Review B **75**, 024511 (2007).
121 H. Sato, A. Tsukada, M. Naito, and A. Matsuda, Physical Review B **61**, 12447 (2000).
122 J. M. Tranquada, B. J. Sternlieb, J. D. Axe, Y. Nakamura, and S. Uchida, Nature **375**, 561 (1995).
123 B. O. Wells, Y. S. Lee, M. A. Kastner, R. J. Christianson, R. J. Birgeneau, K. Yamada, Y. Endoh, and G. Shirane, Science **277**, 1067 (1997).
124 W. Si, H.-C. Li, and X. X. Xi, Applied Physics Letters **74**, 2839 (1999).
125 W. Si and X. X. Xi, Applied Physics Letters **78**, 240 (2001).
126 H. E. Mohottala, B. O. Wells, J. I. Budnick, W. A. Hines, C. Niedermayer, L. Udby, C. Bernhard, A. R. Moodenbaugh, and F.-C. Chou, Nat Mater **5**, 377 (2006).
127 J. Hubbard, Proceedings of the Royal Society of London. Series A. Mathematical and Physical Sciences **276**, 238 (1963).
128 J. B. Goodenough and A. Manthiram, Journal of Solid State Chemistry **88**, 115 (1990).
129 T. Jarlborg, A. Bianconi, B. Barbiellini, R. S. Markiewicz, and A. Bansil, J Supercond Nov Magn **26**, 2597 (2013).
130 I. Bozovic, G. Logvenov, I. Belca, B. Narimbetov, and I. Sveklo, Physical Review Letters **89**, 107001 (2002).
131 H. Sato, A. Tsukada, and M. Naito, Physica C: Superconductivity **408–410**, 848 (2004).
132 G. Ilonca, A. V. Pop, T. Jurcut, C. Lung, G. Stiufiuc, R. Stiufiuc, O. Furdui, E. Mococeanu, and R. Deltour, Modern Physics Letters B **14**, 639 (2000).
133 A. Bianconi, N. L. Saini, A. Lanzara, M. Missori, T. Rossetti, H. Oyanagi, H. Yamaguchi, K. Oka, and T. Ito, Physical Review Letters **76**, 3412 (1996).
134 S. D. Conradson, I. D. Raistrick, and A. R. Bishop, Science **248**, 1394 (1990).

VITA

Lu Jiang was born on May 19th, 1987, in Wuhan, Hubei Province, China. She received his Bachelor of Science Degree from Wuhan University, Beijing in June, 2009, in the ma jor of Materials Physics. She began her Doctor of Philosophy study in Department of Astronomy and Physics from August 2009, in the University of Tennessee, Knoxville.